Atomistic insights on enhanced passivity: DFT study of substitutional Mo on Cr2O3 and Fe2O3 surfaces

Xian Huang, Dominique Costa, Boubakar Diawara, Vincent Maurice, Philippe Marcus

Author preprint published in Corrosion Science
https://doi.org/10.1016/j.corsci.2023.111543

Atomistic insights on enhanced passivity: DFT study of substitutional Mo on Cr_2O_3 and Fe_2O_3 surfaces

Xian Huang, Dominique Costa*, Boubakar Diawara, Vincent Maurice, Philippe Marcus*

PSL Research University, CNRS - Chimie ParisTech, Institut de Recherche de Chimie Paris, Physical Chemistry of Surfaces Group, 11 rue Pierre et Marie Curie, 75005 Paris, France.

* Corresponding authors: dominique.costa@chimieparistech.psl.eu (D. Costa) and philippe.marcus@chimieparistech.psl.eu (P. Marcus).

Abstract

Substitution of a metal cation by Mo and its effects on vacancy formation on (0001)-oriented chromia and hematite surfaces were studied using DFT calculations to provide atomistic insights on the experimentally observed Mo-enhanced passivity. The substitution is favoured energetically, resulting in Mo more enriched in the Fe-rich than in the Cr-rich oxide zones in passive oxide films. The presence of substitutional Mo disfavours the formation of O vacancies and favours metal vacancies, more significantly in Fe_2O_3 than in Cr_2O_3, suggesting a prevention of passivity breakdown in chloride-rich environment and a cure of the Fe-rich weak sites of passivity by Mo.

Keywords

(A) stainless steel, (B) DFT, (C) passive films, (C) Mo effects, (C) vacancies

1. Introduction

The corrosion resistance of many Cr-containing alloys (including Ni-based alloys [1], stainless steels [2], and high entropy alloys [3]) relies on the nanometre-thick native or passive oxide films naturally or electrochemically formed on the surface and protecting the substrate from corrosive attack by the environment. These oxide films are most commonly composed of an inner barrier layer mainly containing chromium oxide and an outer layer containing oxides and hydroxides [1–3]. The inner barrier layer may present weak sites of corrosion protection, locally depleted in Cr and enriched in Fe, and originating from the build-up of oxide film in the early

stages of oxidation as revealed on stainless steel surfaces [4,5]. It is well known that the addition of Mo in these alloys enhances the resistance to breakdown of the passive film and to the initiation of localized corrosion, especially in aggressive Cl-containing environments. In a recent study of the enhanced passivity of Mo-bearing multi-principal element alloys (Cr-Fe-Co-Ni-Mo) [6,7], molybdenum oxide was found enriched mainly as Mo(VI) in the outer layer, and as Mo(IV) concentrated at the inner/outer layer interface including where the Fe-rich weak sites of the inner layer are exposed (Figure 1.a). It was proposed that the addition of Mo may reinforce the protection provided by the inner barrier layer by curing these Fe-rich weak sites of passivity [6]. However, the mechanisms for this curing effect are still not well understood. In order to understand the detailed mechanisms, more investigations of the Mo effects are needed, including atomistic modelling of the interaction of Mo with chromium and iron oxide surfaces.

Simulations in the frame of quantum mechanics, such as Hartree-Fock (HF) method and density functional theory (DFT), are powerful techniques to study materials at the atomic scale. The energies of low-index surfaces of chromia (α-Cr_2O_3 phase of corundum structure) have been calculated using HF method [8], indicating that the $(01\bar{1}2)$ orientation is the most stable in agreement with high-resolution transmission electron microscopy observation on sintered Cr_2O_3 [9]. As for surfaces of hematite (α-Fe_2O_3 phase also of corundum structure), a DFT+U calculation has suggested the (0001) surface as the most stable orientation [10]. Since the ultrathin Cr_2O_3 oxide film grown on Cr(110) [11] and the inner barrier layers of the oxide films formed on Cr(110) [12,13], FeCr(110) [14] and FeCrNi(100) [15] are oriented to the [0001] direction according to the results of low-energy electron diffraction (LEED) and scanning tunneling microscopy (STM), the (0001) surface is more of interest here.

Using M for Cr or Fe metal, the (0001) surface can be double-M-terminated ($-O_3M_2$), single-M-terminated ($-O_3M$), chromyl- or ferryl-terminated ($-O_3MO$) or O-terminated ($-M_2O_3$). The single-M termination is the most often considered in simulations since it possesses null dipole moment for each repeatable stacking unit (M-O_3-M) according to the Tasker classification [16]. The surface phase diagrams for chromia and hematite have been calculated using surface energies obtained from DFT calculations [17,18]. When the oxygen potential increases, the most stable termination changes from single-M-terminated to chromyl- or ferryl-terminated, and then to O-terminated-like ($-O_3Cr_3O_3$ or $-O_3Fe_3O_3$) at zero oxygen potential. By using DFT+U method, Rohrbach *et al*. [18] found that the O-terminated-like surfaces are strongly disfavoured and the chromyl- or ferryl-terminated surfaces become the most stable at zero oxygen potential. Using different exchange-correlation functionals or different Hubbard parameters [19–21], different terminations were found favourable at zero oxygen potential, indicating an important influence of the simulation method on the surface phase stability. In the experiments including electron energy loss spectroscopy (EELS) and ion scattering spectroscopy (ISS) [22], synchrotron X-Ray diffraction (SXRD) [23] and STM [11], single-M termination was observed on the surface of chromia films grown by oxidation on Cr(110) [11,22,23] and bulk hematite [24], while O termination were reported on the surface of hematite film epitaxially grown on Pt(111) [25].

On a single-M-terminated (0001) surface, the terminating metal atom can locate on three kinds of sites. Structural rearrangement between these sites [26] and complicated configurations [23] have been observed experimentally on chromia surfaces. To be simple, the terminating metal atom is usually considered on the same site as in the bulk, which was suggested as the most stable site on chromia surfaces by LEED analysis coupled with empirical potential calculations [27]. In this configuration, a strong contraction (compared to bulk) of the interlayer distance between terminating M and first O layer (50 ~ 63% for chromia [18,23,27,28] and 27 ~ 79% for hematite [18,24]) is often reported from both experiments and calculations. The interlayer distance between first O layer and second M layer was found slightly expanded (0 ~ 12%) [18,24,27,28] except for chromia surfaces in experiments (contracted 3 ~ 20 % [23,27]).

Very few studies have addressed Mo effects on chromia and hematite surfaces [29,30]. Mo doping has been simulated on the Fe_2O_3 surface for studying its effect on the nitrogen reduction reaction [29]. Regarding corrosion resistance, Ng *et al.* [30] have investigated Mo effects on hydrous (0001) surfaces of chromia and hematite with an OH termination using DFT+U. It was found that on Mo-free surfaces, the energies needed to activate the oxygen reduction reaction are higher on the chromia than on the hematite surface, suggesting a better resistance on the chromia surface for a corrosion reaction under cathodic control. After substitution of Cr or Fe by Mo, the activation energies on both surfaces increase, suggesting that substitutional Mo may reinforce the corrosion resistance by slowing down the counterpart cathodic activity.

The formation of intrinsic point defects has been well studied in bulk chromia and hematite and recent studies have summarized the calculations performed using different techniques [31,32]. On surfaces, intrinsic point defects are also involved [33–37]. Nguyen *et al*. [33] have investigated vacancies on hematite surfaces, but only in the outermost and near outermost surface atom layers. Pang *et al*. [34] have reported a surface reconstruction resulting from the creation of O single and Fe-O pair vacancies on hematite surfaces, where the outermost iron layer previously above the outermost oxygen layer was displaced into the subsurface by structural relaxation. It was also reported that increasing the U parameter in DFT+U study increases the formation energies of Fe and O vacancies [34]. Regarding Mo effects on surfaces containing intrinsic point defects, it has not yet been studied whilst the chromia-enriched inner layer protective against corrosion is often considered to grow via the diffusion of intrinsic defects [38].

Here we report on substitutional Mo effects on (0001)-oriented surfaces of chromia and hematite (α-Cr_2O_3 and α-Fe_2O_3 phases hereafter denoted as Cr_2O_3 and Fe_2O_3, respectively) simulated by DFT+U calculations. The thermodynamic framework in which our study was carried out is first explained, then the study of bulk materials and perfect surfaces is presented before investigating substitution by Mo on neutral and charged surfaces. This is followed by reporting the study of vacancy formation on Mo-free and Mo-substituted surfaces. The work provides atomistic insights into the mechanisms by which Mo may enhance the stability of the inner barrier layers of passive films formed on the surfaces of stainless steel and other Cr-containing alloys.

2. Method

2.1. Thermodynamic model

The native or passive oxide films formed on Cr-containing alloys under air or aqueous solutions, respectively, [1–3] contain generally an inner barrier layer markedly enriched in chromium oxide and an outer layer formed by oxides and hydroxides of chromium and other alloying elements. Figure 1.a illustrates such a chemical duplex structure reported for the passive film formed on a Cr-Fe-Co-Ni-Mo multi-principal element alloy [6]. To simplify the calculation of defect formation energies, gaseous environment containing O_2 is considered through an atomistic thermodynamic approach in the present study. Cr_2O_3 (or Fe_2O_3) in contact with the environment is firstly considered before investigating more complex bilayer structures in a further study. Figure 1.b shows the simplified model used in this study and to be compared with the experimental one. To explain how defect formation energy is calculated in the present work, we use Cr_2O_3 as an example. A thick Cr_2O_3 lattice is in contact with gas that contains O_2 on one side (surface) and with a Cr-containing substrate alloy on the other side (interface). The atomic planes of the oxide near surface and interface and those of the alloy near interface may deform due to surface relaxation and crystallographic mismatch.

The effect of pressure on solid state is omitted, and the assumption of perfect gas is used so that the free energy at different pressures can be estimated by that at the standard pressure. The formation entropy is considered negligible with respect to formation enthalpy, and the enthalpies at the standard pressure are approximated by energies at 0 K. With these assumptions, defect formation energy as function of temperature and pressure can be calculated based on DFT energies from ground state calculations.

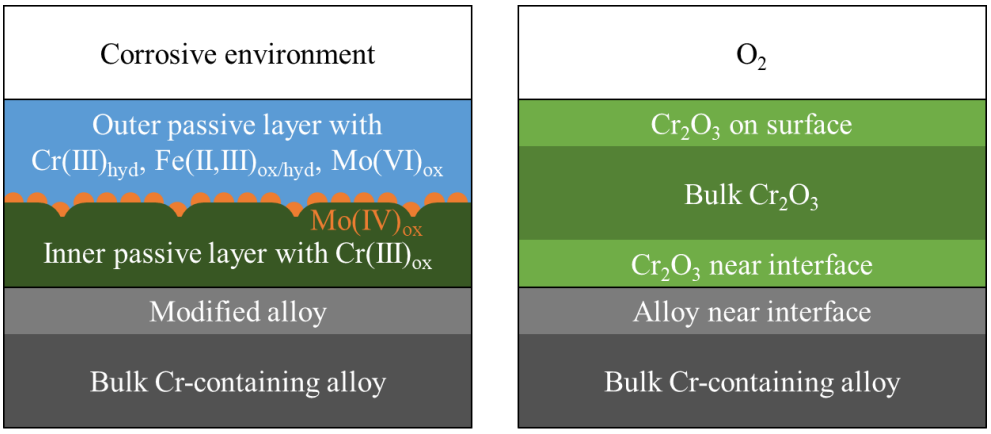

(a) model from the experiments (b) model in simulations

Figure 1. (a) Model of protective oxide films proposed from experiments on Cr-Fe-Co-Ni-Mo multi-principal element alloys [6] and (b) model used in present simulations.

At the alloy/oxide interface, we consider the partial dissociation of the oxide by escape of a Cr atom into the alloy lattice for creation of a Cr vacancy in the Cr_2O_3 lattice. The defect formation reaction and its energy $\Delta_f E_{def}$ for Cr vacancies in the oxide at the interface can be written as:

$$Cr_{2n}O_{3n}(\text{int}) \rightarrow Cr_{2n-1}O_{3n}(\text{int}) + Cr(\text{int}) \quad (1)$$

$$\Delta_f E_{\text{def,int}} = E_{Cr_{2n-1}O_{3n}(\text{int})} - E_{Cr_{2n}O_{3n}(\text{int})} + E_{Cr(\text{int})} \quad (2)$$

where E is the energy (in eV) obtained by DFT calculations, n any integer, and "int" stands for the interface parts of oxide or alloy.

If the difference of energies between interface, surface and bulk are negligible compared to the defect formation energy, then the energies of the oxide and alloy parts near the interface can be estimated by those of the oxide part near surface and of the bulk alloy, respectively. If the heat of mixing of the alloy can be omitted, the energy of Cr in the alloy can be estimated by that of pure Cr metal. With these terms easier to be calculated, Equation (2) is rewritten as:

$$\Delta_f E_{\text{def,int}} = \Delta_f E_{\text{def}} = E_{Cr_{2n-1}O_{3n}(\text{surf})} - E_{Cr_{2n}O_{3n}(\text{surf})} + E_{Cr(\text{bulk})} \quad (3)$$

where "surf" refers to the surface part of the oxide.

On the oxide surface, the formation reaction of Cr_2O_3 between oxide lattice and O_2 in the gas can create 3/2 new O lattice sites for each vacant Cr lattice site in the oxide [38]. Cr vacancies are thus created on the oxide surface according to the following reaction and related defect formation energy:

$$Cr_{2\left(n-\frac{1}{2}\right)}O_{3\left(n-\frac{1}{2}\right)}(\text{surf}) + \frac{3}{4}O_2(\text{gas}) \rightarrow Cr_{2n-1}O_{3n}(\text{surf}) \quad (4)$$

$$\Delta_f E_{\text{def,surf}} = E_{Cr_{2n-1}O_{3n}(\text{surf})} - E_{Cr_{2\left(n-\frac{1}{2}\right)}O_{3\left(n-\frac{1}{2}\right)}(\text{surf})} - \frac{3}{4}E_{O_2} - \frac{3}{4}k_B T \ln\left(\frac{P_{O_2}}{P^0}\right) \quad (5)$$

where k_B is the Boltzmann constant (8.617×10^{-5} eV.K^{-1}), T the temperature in K, P_{O_2} the O_2 partial pressure in atm, and P^0 the standard pressure that equals to 1 atm.

We consider the formation reaction of Cr_2O_3 at the standard pressure:

$$2Cr(\text{bulk}) + \frac{3}{2}O_2(\text{gas}) \rightarrow Cr_2O_3(\text{bulk}) \quad (6)$$

$$\Delta_f H^0_{Cr_2O_3} = E_{Cr_2O_3(\text{bulk})} - 2E_{Cr(\text{bulk})} - \frac{3}{2}E_{O_2} \quad (7)$$

where $\Delta_f H^0$ is the formation enthalpy in eV.

If the simulated surface is thick enough to write the term $E_{\mathrm{Cr}_{2\left(n-\frac{1}{2}\right)}\mathrm{O}_{3\left(n-\frac{1}{2}\right)}(\mathrm{surf})} + \frac{1}{2}E_{\mathrm{Cr_2O_3(bulk)}}$ as $E_{\mathrm{Cr}_{2n}\mathrm{O}_{3n}(\mathrm{surf})}$, then Equation (5) can be rewritten as:

$$\Delta_f E_{\mathrm{def,surf}} = \Delta_f E_{\mathrm{def}} + \frac{1}{2}\Delta_f H^0_{\mathrm{Cr_2O_3}} - \frac{3}{4}RT\ln\left(\frac{P_{\mathrm{O_2}}}{P^0}\right). \quad (8)$$

The same treatment of oxide dissociation or formation can be applied for the creation of O vacancies. At the alloy/oxide interface, the reaction between oxide and alloy lattice and the related defect formation energy for O vacancies can be written as:

$$\mathrm{Cr}_{2\left(n-\frac{1}{3}\right)}\mathrm{O}_{3\left(n-\frac{1}{3}\right)}(\mathrm{int}) + \frac{2}{3}\mathrm{Cr(int)} \rightarrow \mathrm{Cr}_{2n}\mathrm{O}_{3n-1}(\mathrm{int}) \quad (9)$$

$$\Delta_f E_{\mathrm{def,int}} = \Delta_f E_{\mathrm{def}} + \frac{1}{3}\Delta_f H^0_{\mathrm{Cr_2O_3}}. \quad (10)$$

where

$$\Delta_f E_{\mathrm{def}} = E_{\mathrm{Cr}_{2n}\mathrm{O}_{3n-1}(\mathrm{surf})} - E_{\mathrm{Cr}_{2n}\mathrm{O}_{3n}(\mathrm{surf})} + \frac{1}{2}E_{\mathrm{O_2}}. \quad (11)$$

On the oxide surface, an O atom of the Cr_2O_3 lattice could escape into the gas, leaving an O vacancy on the surface:

$$\mathrm{Cr}_{2n}\mathrm{O}_{3n}(\mathrm{surf}) \rightarrow \mathrm{Cr}_{2n}\mathrm{O}_{3n-1}(\mathrm{surf}) + \frac{1}{2}\mathrm{O_2(gas)} \quad (12)$$

$$\Delta_f E_{\mathrm{def,surf}} = \Delta_f E_{\mathrm{def}} + \frac{1}{2}k_{\mathrm{B}}T\ln\left(\frac{P_{\mathrm{O_2}}}{P^0}\right). \quad (13)$$

If a Cr vacancy and a O vacancy are formed together, according to the above equations, the formation energies of the coupled vacancies are

$$\Delta_f E_{\mathrm{def,int}} = \Delta_f E_{\mathrm{def}} + \frac{1}{3}\Delta_f H^0_{\mathrm{Cr_2O_3}} \quad (14)$$

$$\Delta_f E_{\mathrm{def,surf}} = \Delta_f E_{\mathrm{def}} + \frac{1}{2}\Delta_f H^0_{\mathrm{Cr_2O_3}} - \frac{1}{4}RT\ln\left(\frac{P_{\mathrm{O_2}}}{P^0}\right) \quad (15)$$

where

$$\Delta_f E_{\mathrm{def}} = E_{\mathrm{Cr}_{2n-1}\mathrm{O}_{3n-1}(\mathrm{surf})} - E_{\mathrm{Cr}_{2n}\mathrm{O}_{3n}(\mathrm{surf})} + E_{\mathrm{Cr(bulk)}} + \frac{1}{2}E_{\mathrm{O_2}}. \quad (16)$$

If a thermodynamic equilibrium is established at alloy/oxide interface (i.e., no energy is released or absorbed for the formation or dissociation of Cr_2O_3), the equivalent O_2 partial pressure at the equilibrium $P_{O_2,eq}$ (in atm) can be defined [38] by writing the formation enthalpy $\Delta_f H$ (in eV) for the reaction (6) as:

$$\Delta_f H_{Cr_2O_3} = \Delta_f H^0_{Cr_2O_3} - \frac{3}{2} k_B T \ln\left(\frac{P_{O_2,eq}}{P^0}\right) = 0 \,. \quad (17)$$

When the O_2 partial pressure in the gas is as low as the equivalent value at the equilibrium, the defect formation energies on the surface and at the interface are equivalent ($\Delta_f E_{def,surf} = \Delta_f E_{def,int}$).

For substitution at the interface of a metal cation by a foreign atom (e.g., Mo), the same treatment as used to obtain Equation (3) from Equation (2) can be applied to write the substitution reaction and energy as:

$$Cr_{2n}O_{3n}(int) + Mo(int) \rightarrow Cr_{2n-1}MoO_{3n}(int) + Cr(int) \quad (18)$$

$$\Delta_f E_{def,int} = E_{Cr_{2n-1}MoO_{3n}(surf)} - E_{Cr_{2n}O_{3n}(surf)} + E_{Cr(bulk)} - E_{Mo(bulk)} \,. \quad (19)$$

The above treatment was also used for vacancy formation on surfaces containing substitutional atoms and for substitution on surfaces containing vacancies. The same was done for Fe_2O_3 surfaces as for Cr_2O_3 surfaces.

2.2. Calculation details

According to the above formalism, the energies of oxide surfaces with and without Mo and those of pure metals (Cr, Fe and Mo) and oxygen gas are needed to estimate the defect formation energies. The calculated oxide formation enthalpies which could be deduced from the DFT energies of bulk oxides, metals and oxygen gas were used rather than experimental values in order to reduce the systematic errors.

In this study, ground state calculations were performed within the frame of DFT using the Vienna ab initio simulation package (VASP) [39]. Several versions of VASP from 5.3.3 to 5.4.4 were tested and all of them gave nearly the same energy (difference smaller than 10^{-5} eV) when simulating bulk Cr_2O_3 (30 atoms) with experimental structure [40]. The Perdew-Burke-Ernzerhof (PBE) functional using generalized gradient approximation (GGA) [41] was selected as the exchange-correlation functional. The projector-augmented wave (PAW) method [42] was used for treating the pseudopotentials. The projection was done in real space with fully automatic optimization of projection operators unless for calculations of gaseous phase, since it is recommended for large system. For O, the suggested standard version of pseudopotential

was chosen. For Cr, Fe and Mo, the 3*p* semi-core states were treated as valence states in the pseudopotential to obtain higher precision. The overall cutoff energy was set at 520 eV, which corresponds to 1.3 time the highest cutoff energy in the pseudopotentials. Electronic loops were stopped when the difference of energies between two successive iterations was lower than 10^{-6} eV. The default settings were kept for the other parameters which are not involved here.

The DFT+U method using the approach of Dudarev *et al*. [43] was implemented to take into account the strong electronic correlation when calculating localized electronic state such as transition metal oxides. For calculations of metals with delocalized electronic states, the DFT+U method was also used to avoid the systematic error occurring when subtracting a DFT (without U) energy from a DFT+U energy [44]. A discussion of this part is given in the appendix. The parameter *J* for the effective on-site exchange interactions was always 1 eV. For Cr- and Fe-*d* electrons, the parameter *U* for the effective on-site Coulomb interactions was 5 eV as suggested by Rohrbach *et al*. [18]. For Mo-*d* electrons, the parameter U was chosen to be 6 eV so as to obtain good predictions of the electronic properties according to Ding *et al*. [45]. The one-centre PAW charge densities were passed through the charge density mixer up to a l-quantum number of 4, as recommended for DFT+U calculations treating *d*-electrons in order to converge to the ground state more rapidly.

Calculations were performed with collinear spin-polarized configurations for magnetic states. For oxides, no initial magnetic moment was distributed for O since no magnetic moment is measured on O in Cr_2O_3 and Fe_2O_3 [46,47]. For oxygen gas, the initial magnetic moment of O was set to 2 μ_B. For oxides and metals, the initial magnetic moments of 4 and 5 μ_B were distributed for Cr and Fe atoms, respectively, which are slightly higher than their final magnetizations in Cr_2O_3 and Fe_2O_3.

For structure optimizations, the recommended conjugate gradient algorithm was used. During bulk optimizations, the atom positions, cell shape and cell dimensions were relaxed keeping the symmetry of structure fixed, while during surface optimizations, only the atom positions were relaxed. Ionic loops were stopped when the norm of all forces was lower than 10^{-2} eV.Å^{-1}, in which case the difference of energies between two successive iterations was generally lower than 10^{-4} eV. The orbital partial occupancies were treated with the recommended Gaussian smearing method. The width of smearing was set to 0.1 eV since lower smearing width does not bring significant changes to the energy (< 10^{-6} eV) according to a test using bulk Cr_2O_3. According to test results, 3×3×1 and 11×11×11 k-point grids were used for calculations of bulk oxides and metals, respectively. To calculate gases, a cell size of 10 Å with 1 k-point was sufficient.

In order to generate (0001)-oriented surface cell with single-Cr (or -Fe) termination where the terminating metal atoms are in the bulk site position, oxide slabs were created by inserting vacuum with a thickness at least 25 Å in [0001] direction at equidistance of two O layers. A larger vacuum thickness does not significantly change the energy (about 10^{-3} eV) according to a preliminary test. Symmetric (containing 40 and 160 atoms for 1×1 and 2×2 cells, respectively)

and asymmetric slab structures (containing 30 and 120 atoms for 1×1 and 2×2 cells, respectively) were both used in this study. The dipole correction [48] was used for calculations of asymmetric structures in which the bottom surfaces were frozen and the top surfaces were relaxed. According to a test performed with 1×1 Cr_2O_3(0001) surface cell, the dipole correction brings a considerable change of energies of about 0.01 eV for asymmetric structures, but a negligible influence for symmetric structures (~10^{-6} eV). The formation of defects (vacancies and substitutional atoms) was investigated on both surfaces of symmetric structures but only on the top relaxed surface of asymmetric structures. For calculations of bulk and 1×1 (0001) surface cells of Cr_2O_3 and Fe_2O_3, a 3×3×1 k-point grid was used and for calculations of 2×2 (0001) surface cells, a 2×2×1 k-point grid was enough.

Bader charge analysis [49] requires high quality charge density. Compared with the above parameters used for structure optimizations, a denser grid for fast Fourier transformations, a denser k-point grid and another smearing method (tetrahedron method with Blöchl corrections) were tested but yielded the same Bader charges for bulk Cr_2O_3. In consequence, the charge density generated during structure optimizations was used for Bader charge analysis.

3. Results and discussion

3.1. Bulk materials

Both Cr_2O_3 and Fe_2O_3 have the corundum structure in which the O atoms form a hexagonal close packed lattice with 2/3 of the O octahedral sites occupied by Cr or Fe atoms [46,47]. The hexagonal unit cells simulated in this study contained 30 atoms. Figure 2 shows the optimized bulk structures of Cr_2O_3 and Fe_2O_3. The calculated lattice parameters and oxide formation energies were in good agreement with experimental values as shown by Table S1 and Table S2 in the supporting information (SI).

Cr_2O_3 is antiferromagnetic with spins on Cr atoms with commensurate magnetic moment and ↑↓↑↓ order along the [0001] direction [50] if the temperature is below 318 K [51] (Néel temperature); otherwise, it is paramagnetic. The Néel temperature of Fe_2O_3 is about 966 K [52], below which the spins on Fe atoms are perpendicular to the [0001] direction. This configuration could be decomposed into two ferromagnetic sublattices coupled antiferromagnetically, resulting in a small net moment. When the temperature is cooled down to about 260 K [53] (Morin temperature), a reorientation of spins along the [0001] direction with a deviation of about 10° occurs, with a loss of net magnetic moment. In the present work, Fe_2O_3 bulk structures were tested with different spin orientations ([0001], [1000] and [1200]) in collinear spin-polarized calculations, resulting in a difference of energy of only 10^{-8} eV. Consequently, the direction of spins for Fe_2O_3 was set to [0001] direction like for Cr_2O_3 in order to simplify the calculations. The different spin configurations of optimized bulk antiferromagnetic Cr_2O_3 and Fe_2O_3 are shown in Figure 2. The magnetic moments of Cr and Fe in such structures are

3.0 and 4.2 μ_B, respectively, close to the experimental values in the literature (2.7 [46] and 4.2 [47] μ_B, respectively).

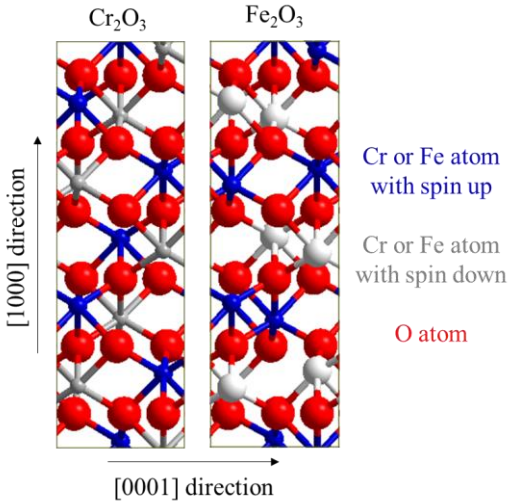

Figure 2. Optimized bulk structures of Cr_2O_3 and Fe_2O_3. O atoms are in red, spin up Cr and Fe atoms in blue, and spin down Cr and Fe atoms in light grey or white. Cell contour is marked by a black line.

In bulk Cr_2O_3 and Fe_2O_3, both metal atoms (Cr and Fe) have a Bader charge of about +1.8 *e* and O atoms have a Bader charge of about -1.2 *e* where *e* is the elementary charge. The formal charges in these oxides are supposed to be +3 *e* for the metal atoms and -2 *e* for O. Thus, a ratio about 0.6 between Bader and formal charges is found for these corundum structures, close to the ratio of 0.56 found in another DFT study for Cr_2O_3 [54]. The conversion ratio of 0.6 is systematically used in the following.

3.2. Perfect surfaces

Here we are interested in the (0001) surfaces of Cr_2O_3 and Fe_2O_3 with single-M termination, where the terminating metal atoms are in their bulk site positions. Two kinds of slab structures were used for simulation: (i) symmetric slabs with both top and bottom surfaces relaxed, which requires more calculation resources, and (ii) asymmetric slabs with unrelaxed bottom surface and relaxed top surface, which requires dipole correction [48] not available for calculations of charged slabs. Both slab structures gave the same surface energy and relaxation if the slab model was thick enough. As shown in Figure 2, the bulk hexagonal cell could be considered as a structure piling up 6 M-O_3-M unit layers. For symmetric slabs, a thickness of 8 unit layers (40 atoms in total for a 1×1 slab) was enough for surface relaxation. All unit layers were relaxed here and even the 2 unit layers nearest to the symmetric centre (one above and one below) could be frozen without affecting the surface relaxation. For asymmetric slabs, 4 unit layers on top were relaxed and 2 unit layers at the bottom were frozen (30 atoms in total for a 1×1 slab). Both complete slab structures are shown in Figure S1 while Figure 3 enlarges the relaxed Cr_2O_3 and

Fe_2O_3 (0001)-oriented surface cells with the denomination of atomic layers used hereafter. Except for the terminating layers of Cr and Fe (Cr1 and Fe1, respectively), "up" and "dn" are used to indicate the metal atoms closer to surface and bulk, respectively, in the same metal atom layer. To reduce the main text, surface energy (Table S3) and relaxation (Table S4) are presented in SI.

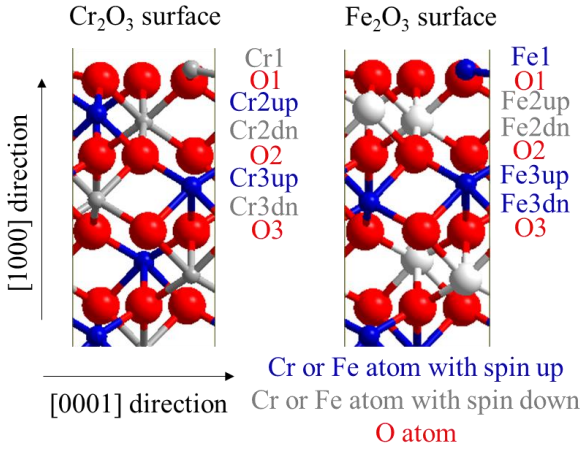

Figure 3. Optimized (0001) surface cells of Cr_2O_3 and Fe_2O_3. O atoms are in red, spin up Cr and Fe atoms in blue, and spin down Cr and Fe atoms in light grey or white. Cell contour is marked by black line.

The formation of Cr_2O_3 and Fe_2O_3 (0001)-oriented surfaces reduces the coordination number of Cr and Fe from 6 (in bulk) to 3 (in terminating layer), which influences the charge distribution. Figure 4 shows the change of Bader and formal charge for the atoms involved by the surface formation. Compared to bulk, only the outermost atomic layers are affected by surface effects for both Cr_2O_3 and Fe_2O_3. The formal charges decrease about 0.2 *e* and 0.25 *e* for "Cr1" and "Fe1" atoms, respectively, and increase about 0.1 *e* for "O1" atoms. The evolution of formal charge on the other atoms is not significant (< 0.1 *e*). In experiments, Cr^{2+} was reported on the surface of (111)-oriented Cr_2O_3 films grown on (110) Cr by EELS and X-Ray photoelectron spectroscopy (XPS) [55]. However, it was re-assigned to Cr^{3+} in a later article [26] based on the results of *ab initio* calculations. In an *ab initio* embedded cluster calculation [56], Mulliken charges of Cr and O were found to be +3 *e* and -2 *e* in bulk Cr_2O_3 and +2 *e* and -1.67 *e* in the topmost layers, respectively, resulting in a variation of -1 *e* and +0.33 *e*. But in another calculation using HF method [28], the variation of Mulliken charge on terminating Cr atoms surface was found to be -0.188 *e*, close to our calculations. The partial reduction of formal charge of about -0.2 *e* calculated in the present work for terminating metal atoms is then considered reasonable.

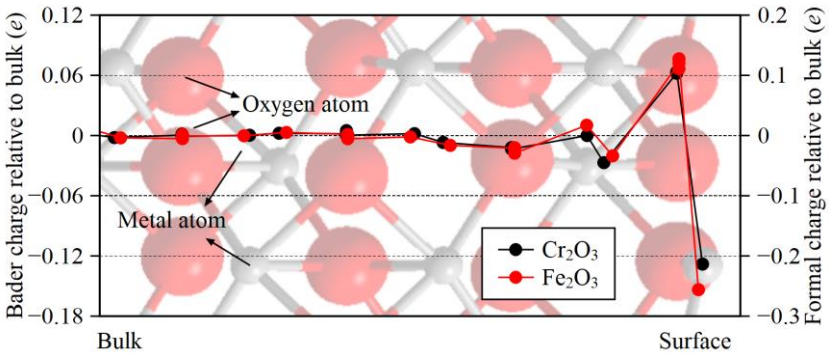

Figure 4. Bader and formal charges of Cr_2O_3 and Fe_2O_3 (0001) surfaces relative to bulk values. Each point represents an atomic layer whose nature is indicated by the background image of the perfect Cr_2O_3 surface according to the [0001] coordinate. O atoms are in red and metal atoms in grey.

3.3. Substitutional Mo effects

In order to introduce Mo, a metal atom M (representing Cr or Fe) was replaced by a Mo atom. One site is substituted on each relaxed surface cells on 1×1 and 2×2 slabs for Cr_2O_3 and Fe_2O_3. Simulations are first performed on neutral surfaces to study the substitution energy and then on surfaces positively charged in order to investigate the oxidation state of substitutional Mo. The latter correspond to electrochemical passivated interfaces under anodic polarization.

3.3.1. Neutral surfaces

Different substitutional sites from the “M1” site in the terminating layer to the “M3dn” site in the third metal layer (Figure 3) were tested on neutral surfaces. The substitutional Mo could have the same or inverse spin orientation as the substituted metal atom. According to a test with the 1×1 Cr_2O_3(0001) surface cell, the substitution of Cr by a Mo atom with the same spin orientation was found to be energetically more favourable than substitution with opposite spin orientation, whatever the substitution site. The calculations were then performed with the “same spin” configuration. Mo substitution did not visibly influence the surface structures after relaxation.

Figure 5 shows the Mo substitution energies obtained on the different tested sites, whose positions are illustrated in Figure 3. No significant difference of energies was found between 1×1 and 2×2 surface cells for Cr_2O_3 and Fe_2O_3. Mo substitution was found to be always exothermic which appears consistent with experiments that report Mo enrichment in native and passive films formed on Mo-containing substrate alloys, including in the Cr-rich inner oxide layer [1–3]. Noteworthy is the result that Mo substitution is always more energetically favoured on the Fe_2O_3 surface than that on the Cr_2O_3 surface. This supports the hypothesis that Mo could stabilize the Fe-rich (Cr depleted) weak sites of protection present in the inner layer by

preferentially substituting Fe as previously proposed [6].

When the substitution site changes from "M1" to "M2up", a decrease of energy is observed for Fe_2O_3 but not for Cr_2O_3. The most favoured site for Mo substitution is the "M2dn" site on both Cr_2O_3 and Fe_2O_3 surfaces, which corresponds to the lower metal atom on the 2nd metal layer from the surface. This result is consistent with a study of dopants in Fe_2O_3 [35] that conclude that small dopants (< 1.7 A) with valences higher than Fe, which is the case for Mo, tend to be located on the subsurface rather than on the topmost surface. For unrelaxed substitution on the relaxed 1×1 Cr_2O_3 surface (i.e. same coordinates between substitutional Mo and substituted Cr), "Cr2dn" is still the most favoured site. However, for unrelaxed substitution on the unrelaxed 1×1 Cr_2O_3 surface (i.e. same coordinates between the atoms on the surface and those in the bulk), the most favoured site becomes the "Cr1" site, which corresponds to the terminating metal atom. This comparison suggests that the surface relaxation, that decreases the interlayer spacing between terminating metal layer and 1st oxygen layer (see SI), stabilizes the substituted terminating metal layer. Substitution by Mo on the most favourable "M2dn" site was also tested with different surface sizes from 1×1 to 3×3 in order to simulate the effect of concentration, but as shown by Figure S2 in SI, the concentration effect is negligible (difference of energies about 0.05 eV) compared to the effect of substitution site.

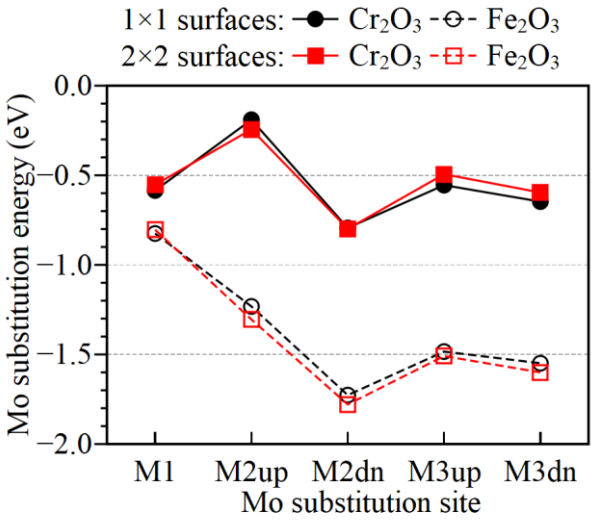

Figure 5. Mo substitution energy from terminating "M1" site in the topmost layer to "M3dn" site in the 3rd metal layer calculated with 1×1 and 2×2 Cr_2O_3 and Fe_2O_3 (0001) surface cells.

Figure 6 shows the changes of Bader and formal charges caused by Mo substitution on the most favourable site "M2dn" calculated with 2×2 surface cells. The variation of charge is mainly located on the substitutional Mo atom and is negligible for the other atoms. Compared with the charges of the substituted metal atoms, the charges on substitutional Mo are slightly higher (about +0.25 *e* in formal charge). Since the increase of formal charge is much smaller than 1, the substitutional Mo atoms on the neutral Cr_2O_3 and Fe_2O_3 surfaces can still be considered as in +3 oxidation state, i.e., carrying approximately the same charge as the substituted metal atoms.

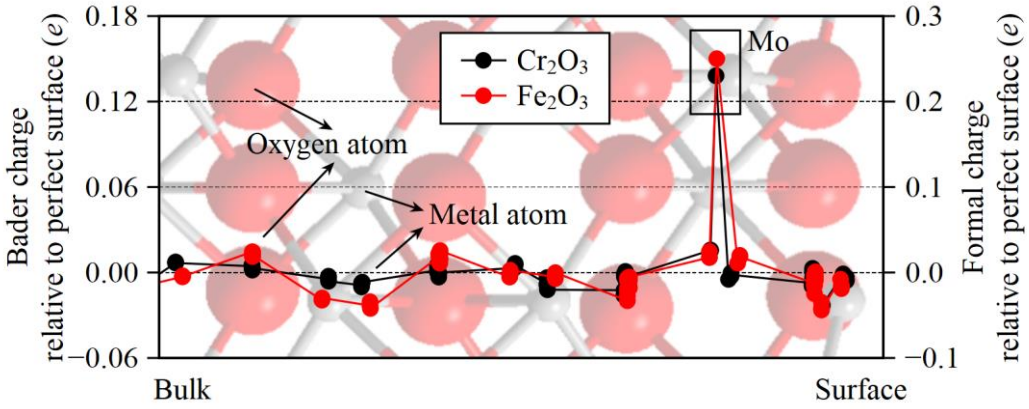

Figure 6. Bader and formal charges of Mo-subtituted Cr_2O_3 and Fe_2O_3 (0001) surfaces relative to the Mo-free surfaces calculated with 2×2 surface cells. Each point represents an atomic layer whose nature is indicated by the background image of the perfect Cr_2O_3 surface according to the [0001] coordinate. O atoms are in red and metal atoms in grey. Formal charges are converted from the Bader charges using the ratio of 0.6.

3.3.2. Charged surfaces

In this part, we consider Mo effects on surfaces positively charged by removal of electrons (addition of positive charge) from the simulated systems, corresponding to electrochemical passivated interfaces under anodic polarization. This allows us to investigate if the substitutional Mo could be in an oxidation state higher than +3 found on neutral surfaces. Symmetric slabs were used to avoid using dipole corrections. On the symmetric slab with 2×2 surface cell, there are two inequivalent configurations for substitution by one Mo on each surface. Both yielded the same energy according to a test on the neutral Fe_2O_3 slab. Therefore, they are not distinguished in the following discussion.

The most favourable sites for substitutional Mo were expected to be the same as on neutral surfaces, which was verified by a test with the 1×1 Cr_2O_3 symmetric slab with 2 added charges. One added charge was localized on each surface and mainly on the substitutional Mo no matter where it substitutes.

Calculations of charged slabs under periodic conditions include the electrostatic interaction between the charged surfaces and their periodic images [57] and their energies cannot be compared directly if the charge distributions are not identical. Thus, we only compare here the Bader charges between the simulated surfaces with different added charges.

Figure 7 shows the changes of Bader and formal charges on Mo-substituted surfaces induced by the addition of positive charge. Added charges are mostly localized on the substitutional Mo atom. In order to estimate the oxidation state, the charges of the substitutional Mo and substituted Cr (or Fe) on perfect surfaces are compiled in Table 1. On the Mo-substituted Cr_2O_3

surface, the 1st added charge is mainly localized on the substitutional Mo (about +0.6 *e* in formal charge), resulting a total formal charge of +3.8 *e*. The 2nd and 3rd added charges are no more localized on the substitutional Mo, but mainly delocalized on the near-surface Cr and O atoms. Mo can then be considered in near +4 oxidation state on all charged surfaces. On the Mo-substituted Fe_2O_3 surface, the behaviour of the first two added charges is like on the Cr_2O_3 surface, while the 3rd added charge is again partially localized on the substitutional Mo (about +0.7 *e* in formal charge), indicating a higher oxidation state (near +5) of Mo in this case. The comparison between the two surfaces shows that substitutional Mo can localize more charge on Fe_2O_3 than on Cr_2O_3 surfaces.

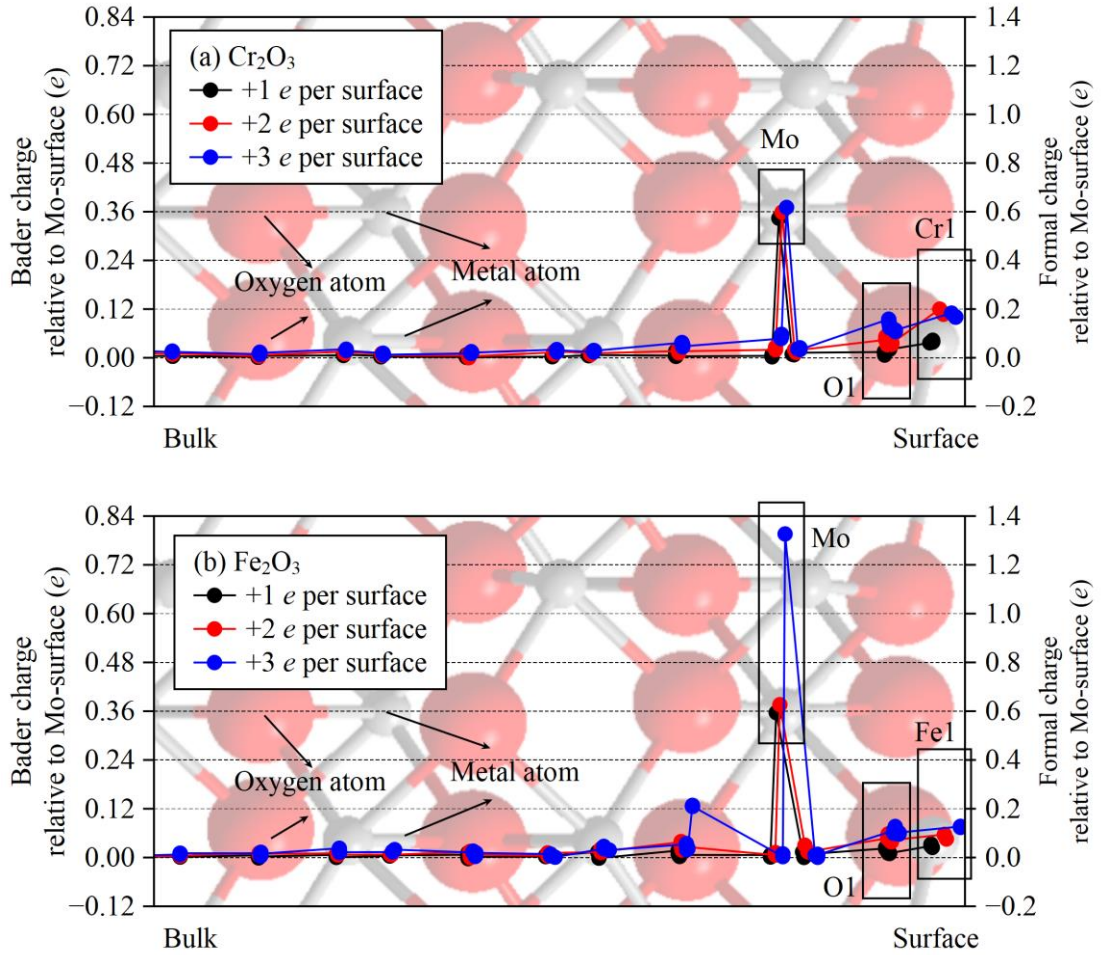

Figure 7. Bader and formal charges of Mo-substituted (a) Cr_2O_3 and (b) Fe_2O_3 (0001) charged surfaces relative to the Mo-substituted neutral surfaces. Each point represents an atomic layer whose nature is indicated by the background image of the perfect Cr_2O_3 surface according to the [0001] coordinate. O atoms are in red and metal atoms in grey. Formal charges are converted from the Bader charges using the ratio of 0.6.

Table 1. Charges (in *e*) on the substituted Cr or Fe atom and substitutional Mo on neutral and charged Cr_2O_3 and Fe_2O_3 (0001) surfaces.

Added charge	Cr_2O_3	Fe_2O_3

	per surface cell	Bader	Formal	Bader	Formal
Substituted atom	+0	+1.8	+3.0	+1.8	+3.0
Substitutional Mo	+0	+1.9	+3.2	+1.9	+3.2
	+1	+2.3	+3.8	+2.3	+3.8
	+2	+2.3	+3.8	+2.3	+3.9
	+3	+2.3	+3.8	+2.7	+4.6

To summarize this section, substitution of Cr or Fe by Mo is exothermic on both perfect surfaces and more favoured on Fe_2O_3 than on Cr_2O_3. The most favoured location of Mo is the "M2dn" site for both. Mo takes the same oxidation degree as the parent metal cation, i.e., +3, unless the system is positively charged. In this case, the 1st positive added charge is mainly localized on the Mo atom, yielding an oxidation state approaching +4. With increasingly positive charging, the Mo oxidation state still increases to between +4 and +6 on Fe_2O_3, but not on Cr_2O_3.

These results suggest that, in the inner oxide layer of a native or passive film in which Cr-rich and Fe-rich oxide zones co-exist:

i) Mo location in a Fe-rich zone is more favoured thermodynamically,

ii) Mo is +3 oxidation state in a non-charged environment and approaches +4 in an electron-depleted environment (corresponding to an anodically polarized interface),

iii) Mo can be further oxidized into an intermediate state between +4 and +6 in the Fe-rich oxide zones of anodically-formed passive film, but not in the Cr-rich oxide zones.

3.4. Vacancy formation

In this section, we discuss first the formation of vacancies on neutral Mo-free surfaces. Three types of vacancies were investigated in the present work: Cr(Fe) single vacancies, O single vacancies and Cr(Fe)-O pair vacancies. The vacancies were created on each relaxed surface of 1×1 and 2×2 slabs for Cr_2O_3 and Fe_2O_3. Secondly, the formation of vacancies was studied on Mo-substituted surfaces, which allows us to investigate the effects of Mo on vacancy formation in the oxide. In the simulations, the substitutional Mo was always placed in the most preferable "M2dn" site according to the previous section.

3.4.1. Mo-free surfaces

For metal atom vacancies, different vacancy sites from terminal "M1" site to sub-surface "M3dn" site of the Cr_2O_3 and Fe_2O_3 surfaces were tested. Figure 8 shows the calculated vacancy formation energies for the different tested sites.

On the Mo-free Cr_2O_3 surface (Figure 8.a), the most favourable sites to create a Cr vacancy are the "Cr2up" sites followed by the "Cr1" sites according to the test with the 2×2 surface cell. The test with the 1×1 surface cell gives a different result: the most favourable site being the "Cr1" site followed by the "Cr2up" site. This disagreement may be due to the remarkable difference of defect concentrations between 1×1 and 2×2 surface cells since one defect was created per surface cell. Indeed, the creation of a Cr vacancy on the "Cr1" site of the 1×1 surface cell completely removes the terminating Cr layer forming an O-terminated surface, which is not the case with the 2×2 surface cell. Another effect comes from structural relaxation. In some cases, reconstruction of the surface structure was observed. Figure 9 shows the first four terminating layers ("Cr1", "O1", "Cr2up" and "Cr2dn") of the relaxed Mo-free 2×2 Cr_2O_3 surface cell with a Cr vacancy on "Cr2up" site. Some "Cr1" atoms (the three "Cr1" atoms nearest to the created vacancy and marked in yellow in Figure 9) are displaced through the "O1" layer into the "Cr2" layer, occupying the octahedral sites of the oxygen sub-lattice initially unoccupied by Cr as seen in Figure 3. Such local rearrangement of the atomic stacking along the [0001] direction (from -Cr-O_3-Cr to -Cr-Cr-O_3) was also observed when creating "Cr2dn" vacancies in the 2×2 surface cell, as shown by Figure S3 in SI, but not for the other sites of Cr vacancies and neither with the 1×1 surface cell. This may be a hint to explain the difference of energy profiles obtained with 1×1 and 2×2 surface cells (Figure 8.a).

On the Mo-free Fe_2O_3 surface (Figure 8.a), both the tests performed with 1×1 and 2×2 surface cells suggest that the most favourable sites to create Fe vacancies are the "Fe3up" sites followed by the "Fe1" sites. Compared to Mo-free Cr_2O_3 surfaces where atomic rearrangement occurred only when creating "M2up" and "M2dn" vacancies, atomic rearrangement of the Mo-free Fe_2O_3 surfaces was observed not only for vacancies on these sites, but also for vacancies created in the deeper sites of the 3rd metal layer as shown in SI (Figure S4). This rearrangement phenomenon may also contribute to decrease the vacancy formation energies for these deep sites, resulting in "Fe3up" site becoming more favoured than the "Fe2up" site for vacancy formation in contrast with Mo-free Cr_2O_3 surfaces.

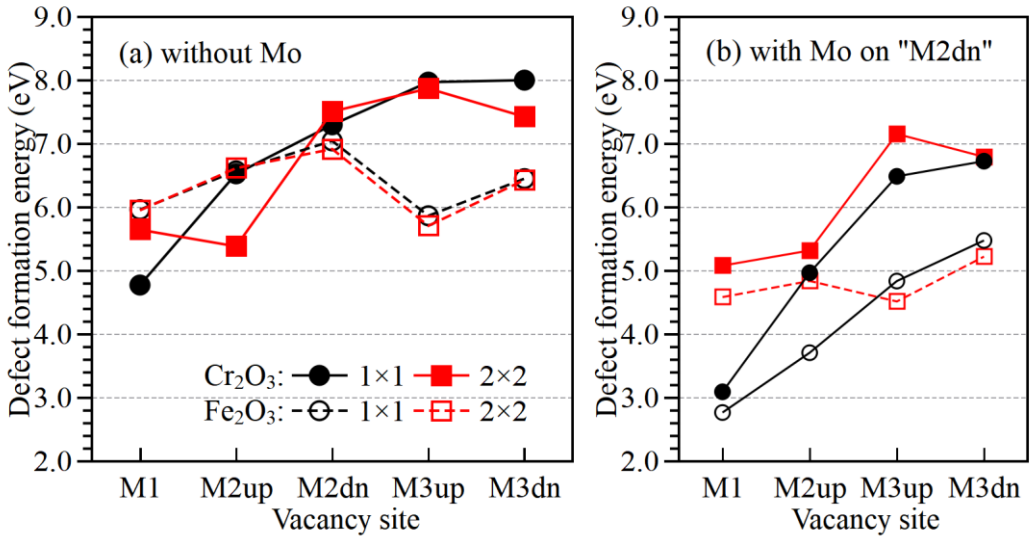

Figure 8. Defect formation energies $\Delta_f E_{def}$ of metal atom vacancies on different sites of Cr_2O_3 and Fe_2O_3 (0001) surfaces (a) without and (b) with substitutional Mo as calculated with 1×1 and 2×2 surface cells and using Equation (3).

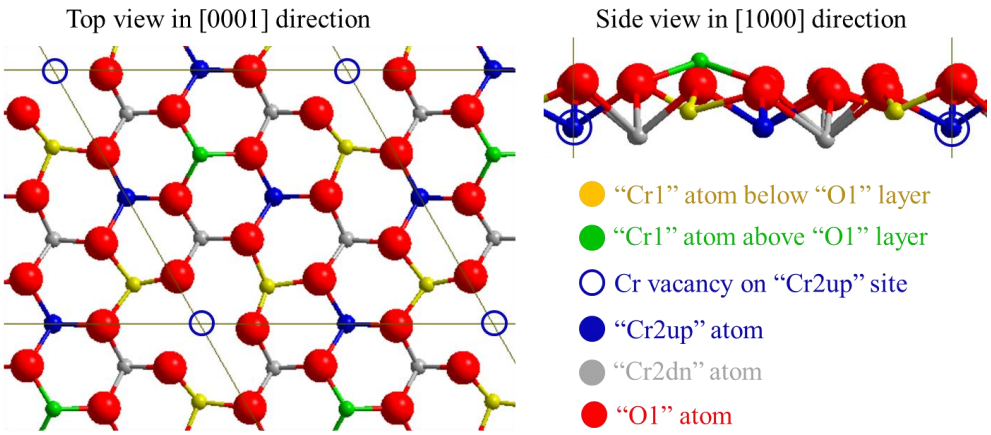

Figure 9. Top and side views of the local rearrangement of the Mo-free Cr_2O_3 (0001) surface structure with a "Cr2up" vacancy observed with a 2×2 surface cell.

Figure 10 shows the O vacancy formation energies obtained on different sites from 1st O layer ("O1" sites) to sub-surface O layers ("O2" and "O3" sites). 1×1 and 2×2 surface cells were tested but little effect of cell size was found, unlike for metal atom vacancies. As a result, only the results obtained with 2×2 surface cells are presented here.

The "O1" sites are the most favorable sites on Mo-free Cr_2O_3 and Fe_2O_3 surfaces. The surface reconstruction leading local rearrangement of atomic stacking, in which the "Fe1" atom is displaced into the "Fe2" layers to stay in the initially unoccupied Fe sites, is observed when creating "O1" or "O3" vacancies on Fe_2O_3 surfaces, as shown by Figure S5 in SI, but no surface reconstruction occurs on Cr_2O_3 surfaces.

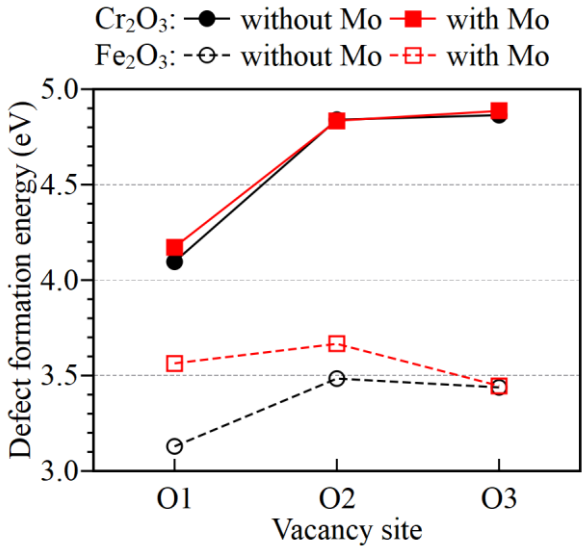

Figure 10. Defect formation energy $\Delta_f E_{\mathrm{def}}$ of oxygen vacancies on different sites of Cr_2O_3 and Fe_2O_3 (0001) surfaces without and with substitutional Mo as calculated with 2×2 surface cells and using Equation (11).

The formation of a metal atom vacancy and an O vacancy nearby (called coupled vacancies here) was also investigated. Since the "Cr1" ("Fe1") sites were found to be nearly always the most favorable, a Cr (Fe) vacancy was created on these sites of the 2×2 Cr_2O_3 (Fe_2O_3) surfaces and an O vacancy was created nearby as coupled vacancy on the "O1" sites, which were also found to be nearly always the most favorable sites for O vacancy formation on both Cr_2O_3 and Fe_2O_3 surfaces. With the existing metal atom vacancy, there are 4 inequivalent "O1" sites to create the O vacancy whose distances to the metal atom vacancy are different. The site closest to the metal atom vacancy was selected here to investigate the formation of couple vacancies. Indeed, according to tests performed on Mo-free Cr_2O_3 and Fe_2O_3 surfaces, the "O1" site closest to the metal atom vacancy on the "Cr1" or "Fe1" site was found the most favorable site to create the coupled vacancies. The defect formation energies are shown by Table S5 in SI and will be further discussed on Mo-substituted surfaces.

3.4.2. Mo-substituted surfaces

Vacancy sites at the same depth should be equivalent for the Mo-free 2×2 surface cell, but the substitutional Mo breaks this symmetry. In this study, only the site the closest to the substitutional Mo was investigated among the vacancy sites at the same depth since the effect of Mo is of interest here.

After substitution by Mo on Cr_2O_3 surfaces on the most favoured "Cr2dn" sites, the most favourable sites for the formation of Cr vacancies become the "Cr1" sites rather than the "Cr2up" sites on the Mo-free surface, indicating that substitutional Mo destabilizes the "Cr1" atoms (Figure 8(b)). A slight repulsion of the "Cr1" atom occurred if the surface was Mo-substituted, which also shows destabilization by the substitutional Mo. Surface reconstruction was observed only for the defective surface with vacancies on "Cr2" atomic layer, like on Mo-free surfaces.

The energy profiles for 1×1 and 2×2 surface cells show the same trend for the Mo-substituted Cr_2O_3 surfaces (Figure 8(b)). However, for the Mo-substituted Fe_2O_3 surfaces, the most favourable sites to create Fe vacancies were found different with 1×1 and 2×2 surface cells still due to the local rearrangement of the atomic stacking. With 2×2 surface cells, the rearrangement was observed except for the defective surface with "Fe1" vacancies, like on Mo-free surfaces. The most favourable sites are also the "Fe3up" sites like on Mo-free surfaces. However, with 1×1 surface cells, the rearrangement was not observed when creating the "Fe3up" vacancies, resulting in vacancy formation energy increasing continuously with sub-surface depth.

For O vacancies, the substitutional Mo on Cr_2O_3 surfaces does not influence significantly the energy profile (Figure 10). On Mo-substituted Fe_2O_3 surfaces, the "O1" and "O2" vacancies,

which are closer to the substitutional Mo atoms than the "O3" vacancies, become less stable than those on Mo-free surfaces. As a result, the most favorable sites to create O vacancies become the "O3" sites closely followed by the "O1" sites. No new surface reconstruction is observed on Mo-substituted surfaces compared to Mo-free surfaces.

The effect of defect concentration was investigated with slab cells of different sizes and containing one vacancy per relaxed surface. Figure 11 compares the defect formation energies for single and coupled vacancies calculated with 1×1, 2×2 and 3×3 Cr_2O_3 surface cells. Energies do not vary when surface size increases beyond 2×2. Considering that larger surface cells consume more calculation resources, the 2×2 surface cell was considered large enough to simulate dilute defects. Substitutional Mo shows a significant effect on the Cr isolated vacancies but not on O isolated vacancies nor Cr-O coupled vacancies.

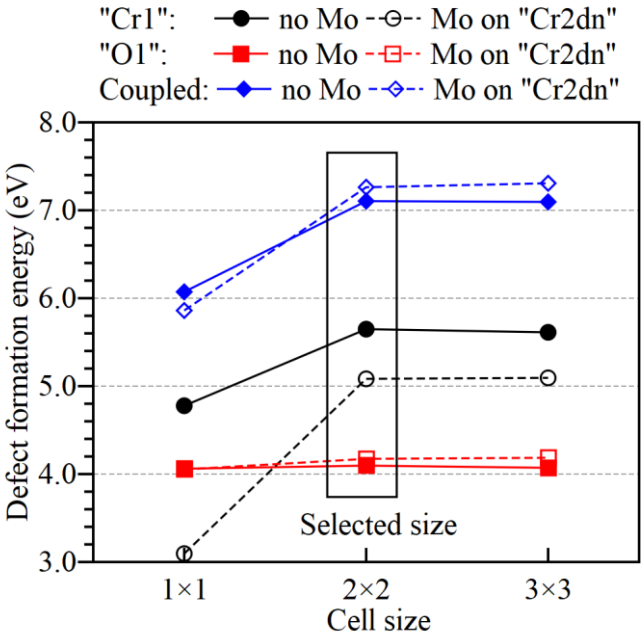

Figure 11. Defect formation energies $\Delta_f E_{def}$ of isolated Cr or O and coupled Cr-O vacancies calculated on Mo-free and Mo-substituted Cr_2O_3 (0001) surfaces of different cell sizes. Cr vacancies are on "Cr1" sites and O vacancies on "O1" sites. Formation energies of Cr, O and coupled vacancies were calculated using Equations (3), (11) and (16), respectively.

Figure 12 shows the vacancy formation energies $\Delta_f E_{def,surf}$ as function of oxygen partial pressure at room temperature (25 °C). The calculated oxide formation energies shown in Table S5 were used to calculate the defect formation energies $\Delta_f E_{def,surf}$ and the equivalent oxygen partial pressures at the equilibrium of formation/dissociation of the oxides. At the thermodynamic equilibrium, O vacancies are expected to be more favourable at low oxygen partial pressure and metal atom vacancies at high oxygen partial pressure [58]. This trend is confirmed in Figure 12 and the coupled metal atom and O vacancies are always less favourable whatever the oxygen partial pressure.

With substitutional Mo, the formation energy of metal atom vacancies becomes lower (-0.57 eV change for Cr vacancies on "Cr1" sites and -1.36 eV for Fe vacancies on "Fe1" sites), indicating that the presence of Mo on the oxide surface is in favour of the formation of metal atom vacancies. The trend is opposite for O vacancies (+0.07 eV on Cr_2O_3 and +0.43 eV on Fe_2O_3 on "O1" sites) and for coupled vacancies (+0.16 eV on Cr_2O_3 and +0.63 eV on Fe_2O_3) but with smaller amplitude. The effect of Mo is more pronounced on the Fe_2O_3 than on the Cr_2O_3 surface.

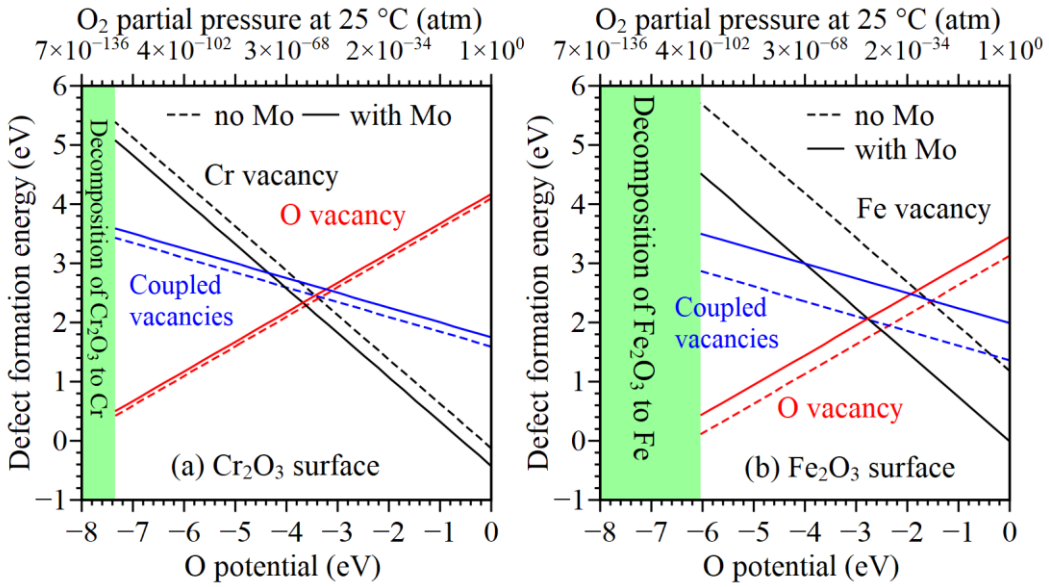

Figure 12. Defect formation energy $\Delta_f E_{\mathrm{def,surf}}$ of vacancies as a function of O_2 partial pressure (O chemical potential) for (a) Cr_2O_3 and (b) Fe_2O_3 (0001) surfaces without and with substitutional Mo. Vacancies are on their most stable sites.

The above content shows the energetical influence of substitutional Mo on vacancy formation. Reversely, Table 2 shows the same trend for the variation of energy for substitution by Mo on "M2dn" sites resulting from the presence of vacancies. Compared to the values for perfect surfaces, the presence of metal atom vacancies favours substitution by Mo on "M2dn" sites. In contrast, O vacancies and coupled vacancies disfavour basically substitution by Mo. The effect is more pronounced on Fe_2O_3 than on Cr_2O_3 surfaces.

Table 2. Energy of substitution by Mo on "M2dn" sites on defective surfaces relative to perfect surfaces. Values on Cr_2O_3 and Fe_2O_3 perfect surfaces are -0.80 and -1.78 eV, respectively.

	Site	Cr_2O_3	Fe_2O_3
Metal atom vacancy	M1	-0.56	-1.37
	M2up	-0.06	-1.78
	M3up	-0.72	-1.19
	M3dn	-0.63	-1.21
Oxygen vacancy	O1	0.08	0.43

	O2	-0.01	0.18
	O3	0.02	0.01
Coupled vacancies		0.16	0.63

The formation of neutral vacancies by removing atoms releases charges that can re-localize on the neighbour atoms. Figure 13 shows the changes of charges on Mo-substituted surfaces resulting from vacancy formation. For metal atom vacancies, the charges released by the removal of cation are localized not only on the substitutional Mo but also on the Cr (Fe) and O atoms and the values are comparable. In contrast, the localization of added charges on the Cr (Fe) and O atoms was tiny relative to that on substitutional Mo on the vacancy-free surfaces (Figure 7). The formation of oxygen and coupled vacancies affects basically the charges of Cr (Fe) and O atoms, but not substitutional Mo.

In order to estimate the oxidation state of the substitutional Mo atom, Table 3 compiles the charges of the substitutional Mo and the substituted Cr on perfect surfaces. According to the charge analysis of neutral perfect surfaces, substitutional Mo is supposed to have a charge state (Mo^{3+}) similar to that of the substituted metal atom. Three positive charges will be released if a Cr (Fe) atom is missing, which may form a Mo^{6+} state. However, the charges localized on the substitutional Mo on Cr_2O_3 surface (+3.7 *e* in formal charge) suggest that substitutional Mo on surfaces containing Cr vacancies is near a Mo^{4+} state. This is consistent with the experimental observation in which Mo observed in the surface oxide film near the inner Cr-rich layer is present as Mo^{4+} rather than Mo^{+6} [6].

When a single metal atom vacancy is created, leaving three positive charges, more released charges are re-localized on Mo on Fe_2O_3 (+1.0 *e* in formal charge) than on Cr_2O_3 (+0.5 *e* in formal charge) surfaces. A similar result was also obtained on vacancy-free charged surfaces (+0.6 *e* on Mo on Cr_2O_3 and +1.4 *e* on Fe_2O_3 in formal charge), indicating that it is easier to transfer the valence electron of Mo to Fe in Fe_2O_3 than to Cr in Cr_2O_3. This is consistent with Allen electronegativity (in Pauling units) defined according to valence electron energies, showing that Fe (1.80) is more electronegative than Cr (1.65) and Mo (1.47) [59,60]. The formal charge on Mo is +0.5 *e* higher on Fe_2O_3 than on Cr_2O_3 for defective surfaces. Since Mo on Cr_2O_3 defective surfaces can be considered as in Mo^{4+} state, one can expect that Mo on Fe_2O_3 surfaces is in intermediate state between Mo^{4+} and Mo^{6+}, even if the formal charge (+4.2 *e*) on Mo on Fe_2O_3 surface is not much higher than +4. Since the oxidation state of Mo can be expected higher than +4 on both vacancy-free charged and vacancy-containing neutral surfaces Fe_2O_3, the intermediate oxidation state between Mo^{4+} and Mo^{6+} observed experimentally [6] may be considered as an indicator of the presence of Mo-substituted Fe-rich local zones in the inner barrier layer of the oxide film (which mostly consists of Cr oxide).

In the study of Larsson *et al*. for passive films on Ni-Cr-Mo alloys [61], Mo^{4+} and Mo^{5+} detected at relatively low potential could be oxidized into Mo^{6+} at more anodic polarization condition. However, it is also reported in the article that Mo^{6+} species may be present as MoO_3, mixed

with $Cr(OH)_3$ and $Ni(OH)_2$ in an amorphous hydrous network, which is not the crystal structure simulated in our DFT calculations. This may explain why the Mo^{6+} state is not found in the present work.

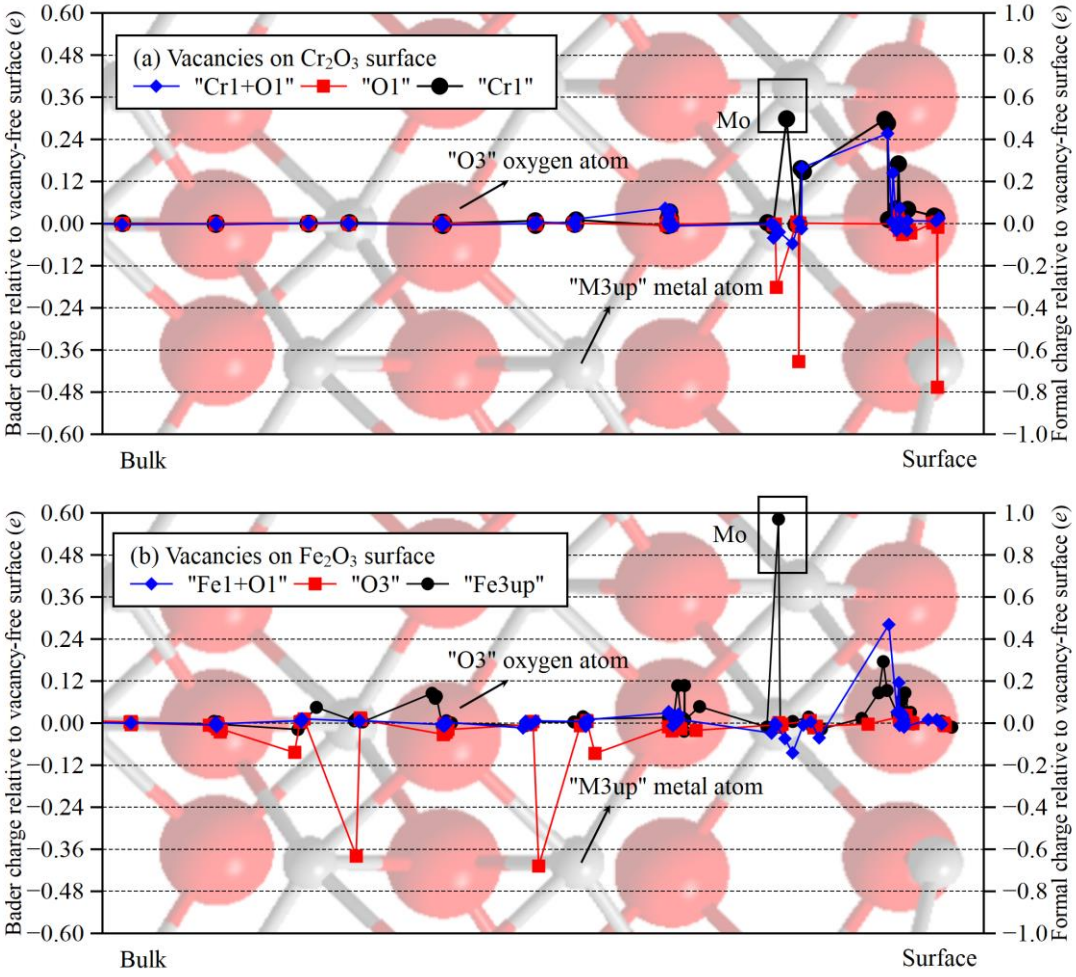

Figure 13. Bader and formal charges of Mo-substituted (a) Cr_2O_3 and (b) Fe_2O_3 (0001) defective surfaces relative to the Mo-substituted vacancy-free surfaces. Each point represents an atomic layer whose nature is indicated by the background image of the perfect Cr_2O_3 surface according to the [0001] coordinate. O atoms are in red and metal atoms in grey. Formal charges are converted from the Bader charges using the ratio of 0.6.

Table 3. Bader and formal charges (in *e*) on substituted Cr (Fe) atom and substitutional Mo atom on vacancy-free and vacancy-containing surfaces. Vacancies are on their most stable sites.

	Vacancy site	Cr_2O_3		Fe_2O_3	
		Bader	Formal	Bader	Formal
Substituted Cr (Fe) atom	Vacancy-free	+1.8	+3.0	+1.8	+3.0
Substitutional Mo	Vacancy-free	+1.9	+3.2	+1.9	+3.2
	Cr1/Fe3up	+2.2	+3.7	+2.5	+4.2

O1/O3	+1.7	+2.9	+1.9	+3.2
Coupled	+1.9	+3.1	+1.9	+3.2

3.5. Implications for passivity

The results of the present work provide insights into the possible mechanism of the enhanced resistance to passivity breakdown and initiation of localized corrosion experimentally observed with Mo-containing stainless steels and other alloys [1–3]. If both Fe-rich and Cr-rich oxide zones coexist on passivated alloys as a result of the local inhomogeneity of the Cr supply in the very first stages of formation of the protective oxide film [4,5], the present work, showing that the energy of substitution by Mo is lower on Fe_2O_3 than on Cr_2O_3 surfaces, suggests that Mo may be locally more enriched in the Fe-rich oxide zones than in the Cr-rich oxide zones. This has implications for the Fe-rich oxide zones, which are the weak sites of protection against corrosive attack, including in the presence of chloride ions.

Obviously, the systems considered here are model systems (corundum structures) and Mo was considered in substitution of Cr and Fe in their crystalline position, whereas other structures and Mo locations could be possible (O sites, unoccupied sites). Mixed oxides could as well as combination of cation and anion vacancies could also be considered. Nonetheless, despite the (over) simplifications of the present models, our results support the hypothesis that Mo heals the Fe rich zones.

Our results suggest that Mo has a negative effect on oxygen vacancy formation and a positive effect on metal atom vacancy formation. The decrease of donor density (which include oxygen vacancies) was indeed reported in the past by Jang and Kwon [62] on passive films on Fe-Cr-Ni and Fe-Cr-Ni-Mo alloys by means of Mott Schottky plots. Our results also partially agree with those of Montemor *et al*. [63] on heat-formed oxide film on 304 and 316 SS, who found that the presence of Mo decreases the density of acceptors and donors in *p*-type Cr- and *n*-type Fe-rich oxide layers, respectively. If intrinsic vacancies are the main defects, the acceptors and donors in *p*-type Cr- and *n*-type Fe-rich oxide layers will be Cr vacancies and oxygen vacancies, respectively. These experimental results seem to be coherent with the negative effect of Mo on oxygen vacancy formation and incoherent with the positive effect on metal atom vacancy formation as concluded in this work. However, the Mott-Schottky plots analyze the entire passive films often containing several kinds of impure oxides and hydroxides in complex multi-layer structures. Comparisons with Mott Schottky plots which give a global measurement on the passive films must be taken with caution.

According to the “point defect model” [64,65] and the generalized model [66] which also considers vacancies, metal cations dissolve in the solution at oxide/solution interface, leaving

metal atom vacancies in the oxide. Since substitution by Mo decreases the formation energy of Fe vacancies more significantly than that of Cr vacancies as shown in the present work, one can expect the selective dissolution of Fe to be accelerated, and thus the replacement of iron oxide by more stable Mo-substituted chromium oxide to be promoted in the oxide film. This replacement mechanism of accelerated selective dissolution would thus contribute to curing the Fe-rich weak sites of passivity.

Cl^- can penetrate in passive oxide films and induce breakdown [67]. It is reported that the presence of O vacancies in Cr_2O_3 favours the penetration of Cl^- from the surface to the subsurface [36]. The present study suggests that substitution by Mo disfavours the formation of O vacancies in Cr_2O_3 and more effectively in Fe_2O_3. This implies that substitutional Mo in passive films could prevent passivity breakdown in chloride-rich environment by reinforcing the Fe-rich weak sites of protection against chloride penetration.

4. Conclusion

Substitution of a metal cation by Mo and its effects on vacancy formation were investigated on (0001)-oriented chromia and hematite surfaces by quantum modelling in order to gain atomistic insight on the enhanced passivity, experimentally observed on Mo-bearing stainless steels and other alloys. The results obtained with DFT+U calculations show that, on neutral and vacancy-free surfaces, substitution by Mo is always exothermic and more favoured energetically on Fe_2O_3 than on Cr_2O_3 surfaces. The charge on the substitutional Mo is only a little higher than that on the substituted metal atom so that the substitutional Mo can be considered as in +3 oxidation state. The 1st added charge on the Mo-substituted surface is mainly localized on the substitutional Mo which can be considered as in +4 oxidation state. The 2nd added charge is delocalized but the 3rd added charge is again localized on the substitutional Mo reaching an intermediate state between +4 and +6. The localization of the 3rd added charge on the substitutional Mo is only observed on Fe_2O_3.

The presence of substitutional Mo favours the formation of metal atom vacancies, but disfavours that of O vacancies or Cr(Fe)-O coupled vacancies. The Mo effect on vacancy formation is more pronounced on Fe_2O_3 than on Cr_2O_3 surfaces. When a metal atom vacancy is created, the released charges localize on the substitutional Mo. More charge is localized on Mo on Fe_2O_3 than on Cr_2O_3 defective surfaces, with the substitutional Mo reaching an oxidation state between +4 and +6 on Fe_2O_3 and only +4 on Cr_2O_3.

The energy of substitution by Mo, lower on Fe_2O_3 than on Cr_2O_3 surfaces, suggests that Mo may be locally more enriched in the Fe-rich than in the Cr-rich oxide zones of the barrier layer of the passive film, and thus could cure the Fe-rich weak sites of the passive film, thus enhancing the corrosion resistance. Since substitution by Mo decreases the formation energy of Fe vacancies more significantly than that of Cr vacancies, the selective dissolution of Fe may be accelerated, resulting in the replacement of iron oxide by more stable Mo-substituted

chromium oxide in the passive film. The effect of substitutional Mo on the formation of O vacancies, more disfavoured on Fe_2O_3 than on Cr_2O_3, implies that Mo could also enhance the corrosion resistance of the passive film in chloride-containing environment by counteracting Cl^- ions penetration via O vacancies.

CRediT authorship contribution statement

Xian Huang: Conceptualization, Methodology, Formal analysis, Investigation, Writing – original draft, Writing – review & editing, Visualization.

Dominique Costa: Conceptualization, Methodology, Validation, Resources, Writing – review & editing, Supervision.

Boubakar Diawara: Conceptualization, Methodology, Software, Validation, Resources, Writing – review & editing, Supervision.

Vincent Maurice: Conceptualization, Methodology, Writing – review & editing, Supervision.

Philippe Marcus: Conceptualization, Methodology, Writing – review & editing, Supervision, Project administration, Funding acquisition.

Declaration of Competing Interest

The authors declare that they have no known competing financial interests or personal relationships that could have appeared to influence the work reported in this paper.

Data Availability

Data will be made available on request.

Acknowledgement

This work was supported by the European Research Council (ERC) under the European Union's Horizon 2020 research and innovation program (ERC Advanced Grant agreement No. 741123).

The authors acknowledge GENCI for high performance calculations in the national CEA centre under the agreement A0040802217 and the HPC resources of MesoPSL financed by the Region Ile de France and the project Equip@Meso (reference ANR-10-EQPX-29-01) of the

programme Investissements d'Avenir supervised by the Agence Nationale pour la Recherche.

Appendix: Energies of chemical references

The energy of the metal is needed as the reference value when creating a defect in its oxide. While the oxide is in localized state that should be calculated in DFT+U method, the metal is in delocalized state that should be calculated without the U effect and systematic error occurs if we subtract the DFT (without U) energy of metal from the DFT+U energy of oxide [44]. The following lists several ways to avoid this situation and their corresponding limits:

1. We can calculate the energy of oxygen gas in DFT and deduce the energy of the metal from the energy of the oxide and the experimental formation energy of the oxide. Oxygen in triplet state is simulated in this case, which is found more stable than in singlet state for O_2 as predicted by experiments [68]. However, the bond energy of dioxygen obtained by DFT calculations is not correct (1.5 eV different from the experimental value [69]) due to the incorrect prediction of the self-interaction effect [70], indicating that the energy of oxygen is not so reliable.

2. We can calculate the energy of metal in DFT+U calculations using the same U parameter as for its oxide. This is the chosen method in the present work. Cr, Fe and Mo metals all have the bcc structure which cubic unit cell contains only 2 atoms. Cr metal is reported in spin density wave (SDW) state but here it is approximated by the antiferromagnetic (AFM) state observed in the literature [71]. Fe and Mo metals are in ferromagnetic (FM) and paramagnetic (approximated by nonmagnetic, NM) states, respectively. All these magnetic states are confirmed by the DFT calculations as the most stable states. However, the atomization energies of metal (shown in Table S6) become incorrect if the metals are calculated in DFT+U.

3. We can use a fitted value for the energy of metal. In this method, several oxides of one metal will be simulated. By using the experimental oxide formation energy, the energy of metal can be fitted with or without fixing the energy of dioxygen. Cr, Fe and Mo have been investigated with this method [72] using different U parameters. New fitting was carried out for this study. Cr_2O_3 and CrO_2, FeO and Fe_2O_3, and MoO_2 and MoO_3 were used for fitting the energies of Cr, Fe and Mo, respectively. Simulation of oxides was globally successful, except that the calculated DOS type of FeO was found metallic while FeO should be a semi-conductor [73]. Table S7 shows the calculation details of the oxides. With or without using a fixed dioxygen energy with a correction of 1.36 eV [44], the difference of fitted energies of metal could attain 1.8 eV (Table S8).

References

[1] Z. Wang, C. Carrière, A. Seyeux, S. Zanna, D. Mercier, P. Marcus, XPS and ToF-SIMS investigation of native oxides and passive films formed on nickel alloys containing chromium and molybdenum, J. Electrochem. Soc. 168 (2021) 041503. https://doi.org/10.1149/1945-7111/abf308.

[2] B. Lynch, Z. Wang, L. Ma, E.-M. Paschalidou, F. Wiame, V. Maurice, P. Marcus, Passivation-induced Cr and Mo enrichments of 316L stainless steel surfaces and effects of controlled pre-oxidation, J. Electrochem. Soc. 167 (2020) 141509. https://doi.org/10.1149/1945-7111/abc727.

[3] X. Wang, D. Mercier, Y. Danard, T. Rieger, L. Perrière, M. Laurent-Brocq, I. Guillot, V. Maurice, P. Marcus, Enhanced passivity of Cr-Fe-Co-Ni-Mo multi-component single-phase face-centred cubic alloys: design, production and corrosion behaviour, Corros. Sci. 200 (2022) 110233. https://doi.org/10.1016/j.corsci.2022.110233.

[4] L. Ma, F. Wiame, V. Maurice, P. Marcus, Origin of nanoscale heterogeneity in the surface oxide film protecting stainless steel against corrosion, Npj Mater. Degrad. 3 (2019) 29. https://doi.org/10.1038/s41529-019-0091-4.

[5] L. Ma, B. Lynch, F. Wiame, V. Maurice, P. Marcus, Nanoscale early oxidation mechanisms of model FeCrNi austenitic stainless steel surfaces at room temperature, Corros. Sci. 190 (2021) 109653. https://doi.org/10.1016/j.corsci.2021.109653.

[6] X. Wang, D. Mercier, S. Zanna, A. Seyeux, L. Perriere, M. Laurent-Brocq, I. Guillot, V. Maurice, P. Marcus, Origin of enhanced passivity of Cr–Fe–Co–Ni–Mo multi-principal element alloy surfaces, Npj Mater. Degrad. 7 (2023) 13. https://doi.org/10.1038/s41529-023-00330-z.

[7] X. Wang, D. Mercier, S. Zanna, A. Seyeux, L. Perriere, M. Laurent-Brocq, I. Guillot, V. Maurice, P. Marcus, Effects of chloride ions on passive oxide films formed on Cr-Fe-Co-Ni(-Mo) multi-principal element alloy surfaces, J. Electrochem. Soc. 170 (2023) 041506. https://doi.org/10.1149/1945-7111/accb10.

[8] J. Sun, T. Stirner, A. Matthews, Structure and surface energy of low-index surfaces of stoichiometric α-Al_2O_3 and α-Cr_2O_3, Proc. 33rd Int. Conf. Metall. Coat. Thin Films. 201 (2006) 4205–4208. https://doi.org/10.1016/j.surfcoat.2006.08.061.

[9] D. Scarano, A. Zecchina, S. Bordiga, G. Ricchiardi, G. Spoto, Interaction of CO with α-Cr_2O_3 surface: a FTIR and HRTEM study, Chem. Phys. 177 (1993) 547–560. https://doi.org/10.1016/0301-0104(93)80032-5.

[10] N. Dzade, A. Roldan, N. de Leeuw, A density functional theory study of the adsorption of benzene on hematite (α-Fe_2O_3) surfaces, Minerals. 4 (2014) 89–115. https://doi.org/10.3390/min4010089.

[11] V. Maurice, S. Cadot, P. Marcus, XPS, LEED and STM study of thin oxide films formed on Cr(110), Surf. Sci. 458 (2000) 195–215. https://doi.org/10.1016/S0039-6028(00)00439-8.

[12] V. Maurice, W.P. Yang, P. Marcus, XPS and STM investigation of the passive film formed on Cr(110) single-crystal surfaces, J. Electrochem. Soc. 141 (1994) 3016–3027. https://doi.org/10.1149/1.2059274.

[13] D. Zuili, V. Maurice, P. Marcus, In situ scanning tunneling microscopy study of the structure of the hydroxylated anodic oxide film formed on Cr(110) single-crystal surfaces, J. Phys. Chem. B. 103 (1999) 7896–7905. https://doi.org/10.1021/jp9911088.

[14] V. Maurice, W.P. Yang, P. Marcus, XPS and STM study of passive films formed on Fe-22Cr(110) single-crystal surfaces, J. Electrochem. Soc. 143 (1996) 1182–1200. https://doi.org/10.1149/1.1836616.

[15] V. Maurice, W.P. Yang, P. Marcus, X-ray photoelectron spectroscopy and scanning tunneling microscopy study of passive films formed on (100) Fe-18Cr-13Ni single-crystal surfaces, J. Electrochem. Soc. 145 (1998) 909–920. https://doi.org/10.1149/1.1838366.

[16] P.W. Tasker, The stability of ionic crystal surfaces, J. Phys. C Solid State Phys. 12 (1979) 4977–4984. https://doi.org/10.1088/0022-3719/12/22/036.

[17] X.-G. Wang, J.R. Smith, Surface phase diagram for Cr_2O_3 (0001) : *Ab initio* density functional study, Phys. Rev. B. 68 (2003) 201402. https://doi.org/10.1103/PhysRevB.68.201402.

[18] A. Rohrbach, J. Hafner, G. Kresse, *Ab initio* study of the (0001) surfaces of hematite and chromia: Influence of strong electronic correlations, Phys. Rev. B. 70 (2004) 125426. https://doi.org/10.1103/PhysRevB.70.125426.

[19] S.M.O. Souvi, M. Badawi, F. Virot, S. Cristol, L. Cantrel, J.-F. Paul, Influence of water, dihydrogen and dioxygen on the stability of the Cr_2O_3 surface: A first-principles investigation, Surf. Sci. 666 (2017) 44–52. https://doi.org/10.1016/j.susc.2017.08.005.

[20] S.M.O. Souvi, M. Badawi, J.-F. Paul, S. Cristol, L. Cantrel, A DFT study of the hematite surface state in the presence of H_2, H_2O and O_2, Surf. Sci. 610 (2013) 7–15. https://doi.org/10.1016/j.susc.2012.12.012.

[21] X. Huang, S.K. Ramadugu, S.E. Mason, Surface-specific DFT + *U* approach applied to α-Fe_2O_3 (0001), J. Phys. Chem. C. 120 (2016) 4919–4930. https://doi.org/10.1021/acs.jpcc.5b12144.

[22] H. Kuhlenbeck, C. Xu, B. Dillmann, M. Haßel, B. Adam, D. Ehrlich, S. Wohlrab, H.-J. Freund, U.A. Ditzinger, H. Neddermeyer, M. Neumann, M. Neuber, Adsorption and reaction on oxide surfaces: CO and CO_2 on Cr_2O_3(111), Berichte Bunsenges. Für Phys. Chem. 96 (1992) 15–27. https://doi.org/10.1002/bbpc.19920960104.

[23] Th. Gloege, H.L. Meyerheim, W. Moritz, D. Wolf, X-ray structure analysis of the Cr_2O_3(0001)-(1×1) surface: evidence for Cr interstitial, Surf. Sci. 441 (1999) L917–L923. https://doi.org/10.1016/S0039-6028(99)00870-5.

[24] M. Lübbe, W. Moritz, A LEED analysis of the clean surfaces of α-Fe_2O_3 (0001) and α-Cr_2O_3 (0001) bulk single crystals, J. Phys. Condens. Matter. 21 (2009) 134010. https://doi.org/10.1088/0953-8984/21/13/134010.

[25] G. Ketteler, W. Weiss, W. Ranke, Surface structures of α-Fe_2O_3 (0001) phases determined by LEED crystallography, Surf. Rev. Lett. 08 (2001) 661–683. https://doi.org/10.1142/S0218625X01001610.

[26] M. Bender, D. Ehrlich, I.N. Yakovkin, F. Rohr, M. Baumer, H. Kuhlenbeck, H.-J. Freund, V. Staemmler, Structural rearrangement and surface magnetism on oxide surfaces: a temperature-dependent low-energy electron diffraction-electron energy loss spectroscopy study of Cr_2O_3(111)/Cr(110), J. Phys. Condens. Matter. 7 (1995) 5289–5301. https://doi.org/10.1088/0953-8984/7/27/014.

[27] F. Rohr, M. Bäumer, H.-J. Freund, J.A. Mejias, V. Staemmler, S. Müller, L. Hammer, K. Heinz, Strong relaxations at the Cr_2O_3(0001) surface as determined via low-energy electron diffraction and molecular dynamics simulations, Surf. Sci. 372 (1997) L291–L297. https://doi.org/10.1016/S0039-6028(96)01255-1.

[28] C. Rehbein, N.M. Harrison, A. Wander, Structure of the α-Cr_2O_3 (0001) surface: An *ab initio* total-energy study, Phys. Rev. B. 54 (1996) 14066–14070. https://doi.org/10.1103/PhysRevB.54.14066.

[29] Z.-Y. Niu, L. Jiao, T. Zhang, X.-M. Zhao, X.-F. Wang, Z. Tan, L.-Z. Liu, S. Chen, X.-Z. Song, Boosting electrocatalytic ammonia synthesis of bio-inspired porous Mo-doped hematite via nitrogen activation, ACS Appl. Mater. Interfaces. 14 (2022) 55559–55567. https://doi.org/10.1021/acsami.2c16081.

[30] M.-F. Ng, D.J. Blackwood, H. Jin, T.L. Tan, DFT study of oxygen reduction reaction on chromia and hematite: insights into corrosion inhibition, J. Phys. Chem. C. 124 (2020)

13799–13808. https://doi.org/10.1021/acs.jpcc.0c03559.

[31] X. Huang, P.C.M. Fossati, L. Martinelli, S. Bosonnet, L. Latu-Romain, Y. Wouters, A DFT study of defects in paramagnetic Cr_2O_3, Phys. Chem. Chem. Phys. 24 (2022) 10488–10498. https://doi.org/10.1039/D1CP05756A.

[32] A. Banerjee, A.A. Kohnert, E.F. Holby, B.P. Uberuaga, Critical assessment of the thermodynamics of vacancy formation in Fe_2O_3 using hybrid density functional theory, J. Phys. Chem. C. 124 (2020) 23988–24000. https://doi.org/10.1021/acs.jpcc.0c07522.

[33] M.-T. Nguyen, N. Seriani, R. Gebauer, Defective α-Fe_2O_3 (0001): an *ab initio* study, ChemPhysChem. 15 (2014) 2930–2935. https://doi.org/10.1002/cphc.201402153.

[34] Q. Pang, H. DorMohammadi, O.B. Isgor, L. Árnadóttir, The effect of surface vacancies on the interactions of Cl with a α-Fe_2O_3 (0001) surface and the role of Cl in depassivation, Corros. Sci. 154 (2019) 61–69. https://doi.org/10.1016/j.corsci.2019.03.052.

[35] Y. Feng, N. Wang, X. Guo, S. Zhang, Characteristics of dopant distribution and surface oxygen vacancy formation for modified Fe_2O_3 in chemical looping combustion, Fuel. 276 (2020) 117942. https://doi.org/10.1016/j.fuel.2020.117942.

[36] K. Oware Sarfo, P. Murkute, O.B. Isgor, Y. Zhang, J. Tucker, L. Árnadóttir, Density functional theory study of the initial stages of Cl-induced degradation of α-Cr_2O_3 passive film, J. Electrochem. Soc. 167 (2020) 121508. https://doi.org/10.1149/1945-7111/abb381.

[37] X. Yin, H. Wang, E.-H. Han, Cl-induced passivity breakdown in α-Fe_2O_3 (0001), α-Cr_2O_3 (0001), and their interface: A DFT study, J. Mater. Sci. Technol. 129 (2022) 70–78. https://doi.org/10.1016/j.jmst.2022.03.034.

[38] D.J. Young, High Temperature Oxidation and Corrosion of Metals, 1st ed., Elsevier, Oxford, UK, 2008. https://www.elsevier.com/books/high-temperature-oxidation-and-corrosion-of-metals/young/978-0-08-044587-8.

[39] G. Kresse, J. Furthmüller, Efficient iterative schemes for *ab initio* total-energy calculations using a plane-wave basis set, Phys. Rev. B. 54 (1996) 11169–11186. https://doi.org/10.1103/PhysRevB.54.11169.

[40] E.E. Newnham, Y.M. De Haan, Refinement of the α Al_2O_3, Ti_2O_3, V_2O_3 and Cr_2O_3 structures, Z. Für Krist. 117 (1962) 235–237. https://doi.org/10.1524/zkri.1962.117.16.235.

[41] J.P. Perdew, K. Burke, M. Ernzerhof, Generalized gradient approximation made simple, Phys. Rev. Lett. 77 (1996) 3865–3868. https://doi.org/10.1103/PhysRevLett.77.3865.

[42] G. Kresse, D. Joubert, From ultrasoft pseudopotentials to the projector augmented-wave method, Phys. Rev. B. 59 (1999) 1758–1775. https://doi.org/10.1103/PhysRevB.59.1758.

[43] S.L. Dudarev, G.A. Botton, S.Y. Savrasov, C.J. Humphreys, A.P. Sutton, Electron-energy-loss spectra and the structural stability of nickel oxide: An LSDA+U study, Phys. Rev. B. 57 (1998) 1505–1509. https://doi.org/10.1103/PhysRevB.57.1505.

[44] L. Wang, T. Maxisch, G. Ceder, Oxidation energies of transition metal oxides within the GGA+U framework, Phys. Rev. B. 73 (2006) 195107. https://doi.org/10.1103/PhysRevB.73.195107.

[45] H. Ding, H. Lin, B. Sadigh, F. Zhou, V. Ozoliņš, M. Asta, Computational investigation of electron small polarons in α-MoO_3, J. Phys. Chem. C. 118 (2014) 15565–15572. https://doi.org/10.1021/jp503065x.

[46] A.H. Hill, A. Harrison, C. Dickinson, W. Zhou, W. Kockelmann, Crystallographic and magnetic studies of mesoporous eskolaite, Cr_2O_3, Microporous Mesoporous Mater. 130 (2010) 280–286. https://doi.org/10.1016/j.micromeso.2009.11.021.

[47] A.H. Hill, F. Jiao, P.G. Bruce, A. Harrison, W. Kockelmann, C. Ritter, Neutron diffraction study of mesoporous and bulk hematite, α-Fe_2O_3, Chem. Mater. 20 (2008) 4891–4899. https://doi.org/10.1021/cm800009s.

[48] J. Neugebauer, M. Scheffler, Adsorbate-substrate and adsorbate-adsorbate interactions of Na and K adlayers on Al(111), Phys. Rev. B. 46 (1992) 16067–16080. https://doi.org/10.1103/PhysRevB.46.16067.

[49] W. Tang, E. Sanville, G. Henkelman, A grid-based Bader analysis algorithm without lattice bias, J. Phys. Condens. Matter. 21 (2009) 084204. https://doi.org/10.1088/0953-8984/21/8/084204.

[50] L.M. Corliss, J.M. Hastings, R. Nathans, G. Shirane, Magnetic structure of Cr_2O_3, J. Appl. Phys. 36 (1965) 1099–1100. https://doi.org/10.1063/1.1714118.

[51] J. Volger, Anomalous specific heat of chromium oxide (Cr_2O_3) at the antiferromagnetic Curie temperature, Nature. 170 (1952) 1027–1027. https://doi.org/10.1038/1701027a0.

[52] M. Białek, J. Zhang, H. Yu, J.-Ph. Ansermet, Antiferromagnetic resonance in α-Fe_2O_3 up to its Néel temperature, Appl. Phys. Lett. 121 (2022) 032401. https://doi.org/10.1063/5.0094868.

[53] L.M. Levinson, Temperature dependence of the weak ferromagnetic moment of hematite, Phys. Rev. B. 3 (1971) 3965–3967. https://doi.org/10.1103/PhysRevB.3.3965.

[54] A. Kumar, F. Ropital, T. de Bruin, B. Diawara, Effects of surface orientations of Cr_2O_3 on CO_2 adsorption: A DFT approach, Appl. Surf. Sci. 529 (2020) 147127. https://doi.org/10.1016/j.apsusc.2020.147127.

[55] C. Xu, M. Hassel, H. Kuhlenbeck, H.-J. Freund, Adsorption and reaction on oxide surfaces: NO, NO_2 on Cr_2O_3(111)/Cr(110), Surf. Sci. 258 (1991) 23–34. https://doi.org/10.1016/0039-6028(91)90897-2.

[56] J.A. Mejias, V. Staemmler, H.-J. Freund, Electronic states of the Cr_2O_3 (0001) surface from *ab initio* embedded cluster calculations, J. Phys. Condens. Matter. 11 (1999) 7881–7891. https://doi.org/10.1088/0953-8984/11/40/319.

[57] H.-P. Komsa, A. Pasquarello, Finite-size supercell correction for charged defects at surfaces and interfaces, Phys. Rev. Lett. 110 (2013) 095505. https://doi.org/10.1103/PhysRevLett.110.095505.

[58] L. Latu-Romain, S. Mathieu, M. Vilasi, G. Renou, S. Coindeau, A. Galerie, Y. Wouters, The role of oxygen partial pressure on the nature of the oxide scale on a NiCr model alloy, Oxid. Met. 88 (2016) 481–493. https://doi.org/10.1007/s11085-016-9670-8.

[59] L.C. Allen, Electronegativity is the average one-electron energy of the valence-shell electrons in ground-state free atoms, J. Am. Chem. Soc. 111 (1989) 9003–9014. https://doi.org/10.1021/ja00207a003.

[60] J.B. Mann, T.L. Meek, E.T. Knight, J.F. Capitani, L.C. Allen, Configuration energies of the d-block elements, J. Am. Chem. Soc. 122 (2000) 5132–5137. https://doi.org/10.1021/ja9928677.

[61] A. Larsson, A. Grespi, G. Abbondanza, J. Eidhagen, D. Gajdek, K. Simonov, X. Yue, U. Lienert, Z. Hegedüs, A. Jeromin, T.F. Keller, M. Scardamaglia, A. Shavorskiy, L.R. Merte, J. Pan, E. Lundgren, The Oxygen Evolution Reaction Drives Passivity Breakdown for Ni–Cr–Mo Alloys, Adv. Mater. (2023) 2304621. https://doi.org/10.1002/adma.202304621.

[62] H. Jang, H. Kwon, In situ study on the effects of Ni and Mo on the passive film formed on Fe–20Cr alloys by photoelectrochemical and Mott–Schottky techniques, J. Electroanal. Chem. 590 (2006) 120–125. https://doi.org/10.1016/j.jelechem.2006.02.031.

[63] M.F. Montemor, A. m. p. Simões, M.G.S. Ferreira, M.D.C. Belo, The role of Mo in the chemical composition and semiconductive behaviour of oxide films formed on stainless steels, Corros. Sci. 41 (1999) 17–34. https://doi.org/10.1016/S0010-938X(98)00126-7.

[64] D.D. Macdonald, The point defect model for the passive state, J. Electrochem. Soc. 139 (1992) 3434–3449. https://doi.org/10.1149/1.2069096.

[65] D.D. Macdonald, The history of the Point Defect Model for the passive state: A brief review of film growth aspects, Electrochimica Acta. 56 (2011) 1761–1772. https://doi.org/10.1016/j.electacta.2010.11.005.

[66] A. Seyeux, V. Maurice, P. Marcus, Oxide film growth kinetics on metals and alloys: I. physical model, J. Electrochem. Soc. 160 (2013) C189–C196. https://doi.org/10.1149/2.036306jes.

[67] P. Marcus, V. Maurice, H.-H. Strehblow, Localized corrosion (pitting): A model of passivity breakdown including the role of the oxide layer nanostructure, Corros. Sci. 50 (2008) 2698–2704. https://doi.org/10.1016/j.corsci.2008.06.047.

[68] P.J. Linstrom, W.G. Mallard, eds., NIST Chemistry WebBook, NIST Standard Reference Database Number 69, National Institute of Standards and Technology, Gaithersburg, MD, 2022. https://doi.org/10.18434/T4D303.

[69] R. D. Johnson III, ed., NIST Computational Chemistry Comparison and Benchmark Database, 2022. http://cccbdb.nist.gov/.

[70] S. Klüpfel, P. Klüpfel, H. Jónsson, The effect of the Perdew-Zunger self-interaction correction to density functionals on the energetics of small molecules, J. Chem. Phys. 137 (2012) 124102. https://doi.org/10.1063/1.4752229.

[71] E. Fawcett, Spin-density-wave antiferromagnetism in chromium, Rev. Mod. Phys. 60 (1988) 209–283. https://doi.org/10.1103/RevModPhys.60.209.

[72] A. Jain, G. Hautier, S.P. Ong, C.J. Moore, C.C. Fischer, K.A. Persson, G. Ceder, Formation enthalpies by mixing GGA and GGA+U calculations, Phys. Rev. B. 84 (2011) 045115. https://doi.org/10.1103/PhysRevB.84.045115.

[73] H.K. Bowen, D. Adler, B.H. Auker, Electrical and optical properties of FeO, J. Solid State Chem. 12 (1975) 355–359. https://doi.org/10.1016/0022-4596(75)90340-0.